Airplane Design Optimization for Minimal Global Warming Impact

Proesmans, P.; Vos, Roelof

DOI
10.2514/1.C036529

Publication date
2022

Document Version
Final published version

Published in
Journal of Aircraft

JOURNAL OF AIRCRAFT
Vol. 59, No. 5, September–October 2022

Airplane Design Optimization for Minimal Global Warming Impact

Pieter-Jan Proesmans* and Roelof Vos†
Delft University of Technology, 2629 HS Delft, The Netherlands

https://doi.org/10.2514/1.C036529

This paper presents a method to assess the key performance indicators of aircraft designed for minimum direct operating costs and aircraft designed for minimum global warming impact. The method comprises a multidisciplinary aircraft optimization algorithm capable of changing wing, engine, and mission design variables while including constraints on flight and field performance. The presented methodology uses traditional class-I methods augmented with dedicated class-II models to increase the sensitivity of the performance indicators to relevant design variables. The global warming impact is measured through the average temperature response caused by several emission species (including carbon dioxide, nitrogen oxides, and contrail formation) over a prolonged period of 100 years. The analysis routines are verified against experimental data or higher-order methods. The design algorithm is subsequently applied to a single-aisle medium-range aircraft, demonstrating that a 57% reduction in average temperature response can be achieved as compared to an aircraft optimized for minimal operating costs. This reduction is realized by flying at 7.6 km and Mach 0.60, and by lowering the engine overall pressure ratio to approximately 37. However, to compensate for the lower productivity, it is estimated that 13% more climate-optimized aircraft have to be operated for the hypothetical fleet under consideration.

Nomenclature

A	=	aspect ratio or cross-sectional area, m^2
b	=	wingspan, m
c	=	chord length, m; or climb rate, m/s
$\bar{c}$	=	length of mean aerodynamic chord, m
C_D	=	aircraft drag coefficient
C_{D_0}	=	zero-lift drag coefficient
C_L	=	aircraft lift coefficient
C_{ops}	=	operating costs, U.S. dollars/(seat · nm) or U.S. dollars
d	=	diameter, m
E_i	=	emission of species i, kg
EI_i	=	emission index of species i, kg/kg
e	=	Oswald factor
h	=	altitude, m or ft
l	=	length, m
M	=	Mach number
m	=	mass, kg
$\dot{m}$	=	mass flow, kg/s
N	=	integer number or amount
p	=	pressure, N/m^2
r_{bl}	=	block range, km
S	=	surface area, m^2
T	=	thrust, kN; or temperature, K
t/c	=	chord thickness
t_{bl}	=	block time, h
U_{ann}	=	annual utilization, h/year
V	=	velocity, m/s
$\bar{V}$	=	volume coefficient
W	=	weight, kN
x	=	absolute, longitudinal coordinate, m
$\boldsymbol{x}$	=	design vector
γ	=	ratio of specific heats
ΔT	=	surface temperature change, K
$\Lambda_{0.25}$	=	wing quarter-chord sweep angle, deg
λ	=	wing taper ratio
ξ	=	longitudinal coordinate relative to the mean aerodynamic chord
ρ	=	density, kg/m^3
χ_i	=	concentration of species i, parts per million volume

Subscripts

AC	=	evaluated for one aircraft
ann	=	annually
app	=	approach condition
core	=	core flow
cr	=	cruise condition
eng	=	engine
FG	=	fuselage group
fe	=	fixed equipment
fleet	=	evaluated for the entire fleet
fuel	=	fuel
fus	=	fuselage
ht	=	horizontal tail
nac	=	nacelle
root	=	chord
TO	=	takeoff condition
tip	=	tip chord
vt	=	vertical tail
WG	=	wing group
w	=	wing
0	=	sea-level condition or initial value
0.25	=	measured at quarter-chord
$*$	=	optimal solution

Presented as Paper 2021-1297 at the AIAA SciTech 2021 Forum, Virtual Event, January 11–15 and 19–21, 2021; received 26 April 2021; revision received 18 February 2022; accepted for publication 19 April 2022; published online 21 June 2022.

*Ph.D. Candidate, Faculty of Aerospace Engineering, Kluyverweg 1; P.Proesmans@tudelft.nl. Student Member AIAA (Corresponding Author).

†Assistant Professor, Faculty of Aerospace Engineering, Kluyverweg 1; R.Vos@tudelft.nl. Associate Fellow AIAA.

I. Introduction

THE fact that aviation contributes to global warming is well established [1,2]. It is estimated that in 2011, aviation resulted in approximately 3.5% of the net anthropogenic effective radiative forcing, of which 66% is caused by non-carbon dioxide (CO_2) contributions: acknowledging the remaining uncertainties [2]. Although this net effect may seem relatively small, it is important to note that the aviation transport industry grows fast as compared to other transport sectors by approximately 4 to 5% annually in terms of revenue passenger kilometers (RPKs) [3,4]: ignoring the potential influence of the Corona virus pandemic in 2020. Hence, technological advancements, operational changes, new policies, or any combination thereof might have to be adopted to reduce aviation's impact. However, radical solutions implemented in land-based

transportation, such electric propulsion, cannot as easily be adopted in commercial aircraft.

Previous studies have revealed that the objective of minimizing the global warming impact, from an aircraft design perspective, does not align with the objective of minimizing direct operating costs (DOCs) [5–7]. Even when the minimization of fuel consumption is considered as the overall design objective, this still does not result in an airframe and engine combination that has a minimal impact on global warming due to non-CO_2 effects [8].

In Ref. [5], Antoine and Kroo carry out a multiobjective optimization of both aircraft and engine design variables for four individual design objectives: minimal DOCs, minimal fuel burn, minimal nitrogen oxides (NO_x) emissions, and minimal noise. In their research, the climate impact of an aircraft was assessed by the emissions (in kilograms or pounds) of CO_2 over the entire flight as well as the NO_x emissions in the landing and takeoff (LTO) cycle. These two cost functions are considered individually because it is assumed that NO_x emissions in cruise are insignificant with respect to the emissions of CO_2 in cruise. Similar approaches were taken by Henderson et al. [9] and Chai et al. [10]. Although the NO_x emissions in LTO are of interest and International Civil Aviation Organization (ICAO) regulations are imposed, this measure does not account for the effect of NO_x at high altitudes due its influence on short-term ozone (O_3) creation and long-term methane (CH_4) and ozone depletion. Such indirect effects on global warming, and other effects such as contrails and contrail cirrus, have to be determined through more advanced climate models and more comprehensive metrics. Examples of the latter are the average temperature response (ATR) [6,7,11] and the global warming potential [12].

Later studies by Dallara and Kroo [7] and Koch [13] included more advanced models and metrics in aircraft optimization routines. The former adopted a linearized climate model with altitude variations, providing an average climate response with limited computational power; whereas the latter employed the more detailed AirClim model by Grewe and Stenke [14]. Although the numerical results of these studies cannot be compared directly, the trends in aircraft design parameters appear to be similar. For example, when changing the design objective from the minimization of DOCs to the minimization of the average temperature response, it can be observed that the wing aspect ratio increases, the wing gets less sweepback, the cruise Mach number reduces, and the cruise altitude is lowered. Although only operational changes, such as a different cruise altitude and Mach number, can already reduce the climate impact of the original aircraft, the financial cost rise can be limited by an optimized redesign.

The studies by Dallara and Kroo [7] and Koch [13] can be further extended by including more turbofan design variables such as the overall pressure ratio (OPR) and the turbine entry temperature (TET). Research conducted in NASA's Environmentally Responsible Aviation (ERA) project, among others, has explored the influence of a higher OPR and an increased bypass ratio (BPR) on the fuel burn, LTO NO_x, and noise [15]. Although it was shown that such engine cycle modifications can yield a significant reduction in fuel burn (33 to 45% for a large single-aisle aircraft), they may have an adverse effect on non-CO_2 climate effects. Raising the OPR and TET, for example, increases the formation of thermal NO_x [16], although the emission index of NO_x in LTO and cruise can be further reduced through future combustor technologies [17]. Additionally, increasing the bypass ratio of turbofan engines increases the probability of contrail formation [18]. This demonstrates that optimizing for minimum fuel burn, again, does not necessarily align with the objective of minimizing global warming impact.

Although flying slower may be one effective measure to reduce the climate impact of an aircraft design, it increases the mission block time. For a constant travel demand, this productivity loss has to be covered by carrying more passengers per flight or by increasing the number of aircraft in the fleet. Several research projects have highlighted the importance of a complete fleet-level analysis in the assessment of new technologies and have proposed advanced modeling frameworks [19–21] in which the aircraft flight profiles have to be simulated [22]. Research by Moolchandani et al. [23] and Jimenez et al. [24] employed fleet-level models to assess the environmental impact of future technologies considered in the ERA project. It was concluded that introduction of ERA technologies can lower the fleet-total fuel burn sufficiently to sustain carbon-neutral operational growth in the future, according to the goals set worldwide, although a discussion of non-CO_2 climate effects is not included.

Building upon these observations from previous research, it is of interest to study what combination of turbofan, airframe, and operational design variables minimizes a comprehensive climate metric while monitoring the potential impact on the fleet operations. The research presented in this paper therefore aims at answering the following question: How do the airplane design variables (defined by wing, engine, and mission design variables) change when shifting from a direct-operating-cost objective toward a climate-impact objective? To answer this question, a design methodology is proposed that is capable of capturing the interrelated effects of all relevant disciplines. Furthermore, the temporal effects of CO_2, NO_x, and induced cloudiness have to be assessed by employing one comprehensive metric. The current scope is limited to a classic tube-and-wing configuration, with kerosene-fueled turbofan engines mounted to the wing and using state-of-the art technology. Other environmental aspects, such as noise and air quality, are not taken into account in the current study.

Although it is recognized that operational changes and trajectory optimizations can further reduce the fuel burn [25,26] and ATR [27], such improved operational schemes are outside the scope of the current study. Nevertheless, it is recommended to perform a simultaneous optimization of the aircraft design and operations to minimize the climate impact, including non-CO_2 effects, in the future by employing similar approaches as were taken in previous studies [23,28].

The paper is structured as follows. Following this Introduction, Sec. II defines the optimization problem and elaborates on the multidisciplinary design methodology. All the relevant analysis methods are explained in this section. Subsequently, validation of the analysis methods is performed in Sec. III along with the verification of the design methodology. Section IV presents the results of the optimization study tailored toward a medium-range single-aisle aircraft, and it answers the research question introduced earlier. Finally, the most important conclusions are gathered in Sec. V along with recommendations for further studies.

II. Problem Formulation and Methodology Description

To answer the research question proposed in the Introduction (Sec. I), a multidisciplinary design and optimization routine is developed. This section discusses the arrangement of the implemented framework tailored to the current research aim. Section II.A focuses on the definition of the optimization problem and the overall strategy, followed by Sec. II.B, which discusses the methods of the individual analyses and design disciplines.

A. Design and Optimization Problem

One can optimize an aircraft design to achieve the minimal average temperature response, minimal cash operating costs (COCs) C_{ops}, or minimal mission-fuel burn m_{fuel}. However, previous research has indicated that these objectives result in different airplane designs with different performance indicators. To study the difference between the three, a single-objective optimization problem is defined as follows:

$$
\begin{aligned}
\underset{\boldsymbol{x}}{\text{minimize}} \quad & F(\boldsymbol{x}) = \text{ATR}_{100}(\boldsymbol{x}) \quad \text{or} \quad C_{\text{ops,fleet}}(\boldsymbol{x}) \quad \text{or} \quad m_{\text{fuel,fleet}}(\boldsymbol{x}) \\
\text{subject to} \quad & W/S \le \frac{1}{2}\rho_0 \left(\frac{V_{\text{app}}}{1.23}\right)^2 C_{L_{\max}}, \\
& b \le b_{\max}, \\
& \text{TET}_{\text{TO}} \le \text{TET}_{\text{TO, max}}, \\
& C_{L_{\text{cr}}} \le \frac{C_{L_{\text{buffet}}}}{1.3} = \frac{0.86 \cdot \cos \Lambda_{0.25}}{1.3}, \\
& C_{L_{\max}} \le 2.8 \cdot \cos \Lambda_{0.25}, \\
& x_i^L \le x_i \le x_i^U \quad \text{for } i = 1, 2, \ldots, 10
\end{aligned} \tag{1}
$$

Table 1 Design variables and their respective bounds and initial values

Variable	Description, unit	Lower bound $\boldsymbol{x}^L$	Upper bound $\boldsymbol{x}^U$
W/S	Wing loading, kN/m^2	3.00	7.00
A	Aspect ratio	5.00	12.0
$C_{L_{\max}}$	Maximum lift coefficient	2.00	2.80
BPR	Bypass ratio	4.00	11.0
Π_{fan}	Fan pressure ratio	1.30	1.70
Π_{lpc}	LPC pressure ratio	1.30	1.70
Π_{hpc}	HPC pressure ratio	10.0	20.0
TET	Turbine entry temperature, K	1100	1700
h_{cr}	Initial cruise altitude, km	6.00	12.0
M_{cr}	Cruise Mach number	0.60	0.80

LPC = Low-pressure compressor.
HPC = High-pressure compressor.

Because the climate impact is assessed for a complete fleet, the costs and fuel usage are evaluated in a similar manner, which is denoted by the fleet subscript. The design vector $\boldsymbol{x}$ contains the variables related to the airframe, engine, and mission. A summary of these variables and their lower $\boldsymbol{x}^L$ and upper $\boldsymbol{x}^U$ bounds is provided in Table 1. For the airframe, the aspect ratio A, wing loading W/S, and maximum lift coefficient $C_{L_{\max}}$ are used as the prime design variables, where the maximum lift coefficient is related to the design of the high-lift devices. The engine design is governed by the bypass ratio, the pressure ratios of the individual compressor elements Π_i, as well as the turbine entry temperature. The mission design variables comprise the cruise Mach number M_{cr} and the cruise altitude h_{cr}.

The optimization definition in Eq. (1) includes five constraints. The first one imposes a limit on the wing loading due to the required minimum approach speed V_{app} at the selected $C_{L_{\max}}$. The single-aisle medium-range jet aircraft of interest is considered to belong to ICAO aircraft approach category C, resulting in an approach speed of approximately 135 to 140 kt (69 to 72 m/s). A constraint is introduced for the maximum turbine entry temperature at takeoff. $\text{TET}_{\text{TO,max}}$ is assumed to be 2000 K according to the insights by Mattingly et al. [29]. The third constraint dictates a maximum wingspan. For the aircraft category under consideration, this limit is set to 36 m.

The fourth constraint restricts the aircraft lift coefficient in the cruise condition due to buffet onset. The lift coefficient at which buffet occurs, for a given sweep angle, is estimated from the buffet onset boundaries provided by Obert [30]. Finally, a constraint is added to limit the maximum achievable lift coefficient. As discussed by Obert, $C_{L_{\max}}$ decreases with an increasing quarter-chord wing sweep angle according to a linear relation with the cosine of this angle. A value of 2.8 relates to the maximum lift coefficient attainable at a zero sweep angle. The latter two constraints are plotted in Fig. 1.

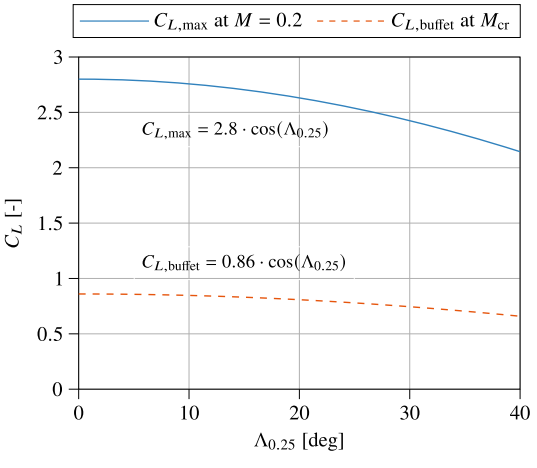

Fig. 1 Constraints on $C_{L_{\max}}$ and $C_{L_{\text{buffet}}}$.

Other flight and field performance constraints are considered in the class-I sizing module (Sec. II.B.1).

The structure of the design and optimization approach is presented in Fig. 2 in the format of an extended design structure matrix (XDSM), as introduced by Lambe and Martins [31]. The airframe and propulsion design disciplines both consist of several design modules, as shown in Figs. 3 and 4. A multiple discipline feasible scheme with a Gauss–Seidel procedure is implemented for this problem with limited complexity. The working principles and assumptions of the individual analysis methods on the diagonal of the XDSM are elaborated on in a subsequent section. In this framework, the optimizer and converger modules are separated. The inner convergence loop ensures that the airplane, defined by the design variables set by the optimizer, is consistent in terms of operating empty mass and maximum takeoff mass.

B. Analysis Methods

As introduced earlier in this paper, answering the research question requires a multidisciplinary approach to capture interrelated effects of design choices. In this subsection, the methodologies and assumptions of these disciplines are discussed in more detail.

1. *Class-I Sizing*

Based on the inputs of the aspect ratio, wing loading, the maximum lift coefficient, cruise altitude, and Mach number, a preliminary sizing study is performed to size the wing area S and the sea-level takeoff thrust T_{TO}. The sea-level thrust-to-weight ratio is computed as the maximum required for three performance conditions: takeoff distance [included through the takeoff parameter (TOP)], cruise Mach number M_{cr} at the beginning of cruise, and the second-segment climb gradient (c/V) in the one-engine-inoperative condition:

$$\frac{T_{\text{TO}}}{W} = \max\left(\frac{W/S}{\text{TOP}}\frac{1}{C_{L_{\text{TO}}}}, \left(\frac{\rho_0}{\rho_{\text{cr}}}\right)^{3/4}\left[\frac{C_{D_0}(1/2)\gamma p_{\text{cr}} M_{\text{cr}}^2}{(W/S)_{\text{cr}}} + \frac{(W/S)_{\text{cr}}}{\pi A e \frac{1}{2} p_{\text{cr}} \gamma M_{\text{cr}}^2}\right], \frac{N_{\text{eng}}}{N_{\text{eng}} - 1}\left(\frac{c}{V} + 2\sqrt{\frac{C_{D_0}}{\pi A e}}\right)\right) \tag{2}$$

Here, TOP is the takeoff parameter, which correlates to the takeoff distance [32]. $C_{L_{\text{TO}}}$ is the takeoff lift coefficient that, in turn, is assumed to be related to the maximum lift coefficient according to

$$C_{L_{\text{TO}}} = C_{L_{\max,\text{TO}}}/1.21 = (C_{L_{\max}} - 0.3)/1.21$$

The value of 0.3 is derived from the different takeoff and landing flap settings. $(W/S)_{\text{cr}}$ is the wing loading at the start of the cruise phase. Furthermore, C_{D_0} and e are the zero-lift drag coefficient and Oswald factor, respectively. Also, γ is the ratio of specific heats and N_{eng} is the number of engines. Note that ρ_{cr} and p_{cr} are the density and pressure at cruise altitude, respectively. These values are dependent on the cruise altitude h_{cr}, which is a design variable in this study. Hence, the pressure and density in Eq. (2) are adapted according to the relations of the International Standard Atmosphere (ISA) model in Table 2 as a function of the cruise altitude set by the optimizer.

2. *Aerodynamics*

The aerodynamic module computes the drag polar of the airplane as a function of its geometry. The geometry is influenced directly by the selected design variables, as well as changes in the engine size. The creation of the geometry is summarized in Appendix C. The aerodynamic discipline provides an update to the estimated drag polar that, in turn, is employed in the propulsion discipline and mission analysis. Furthermore, this polar is also fed back to the class-I sizing module to reevaluate the thrust-to-weight ratio according to Eq. (2).

The drag estimation methods are set up according to the techniques laid out by Obert [30]. The following quadratic drag polar is assumed:

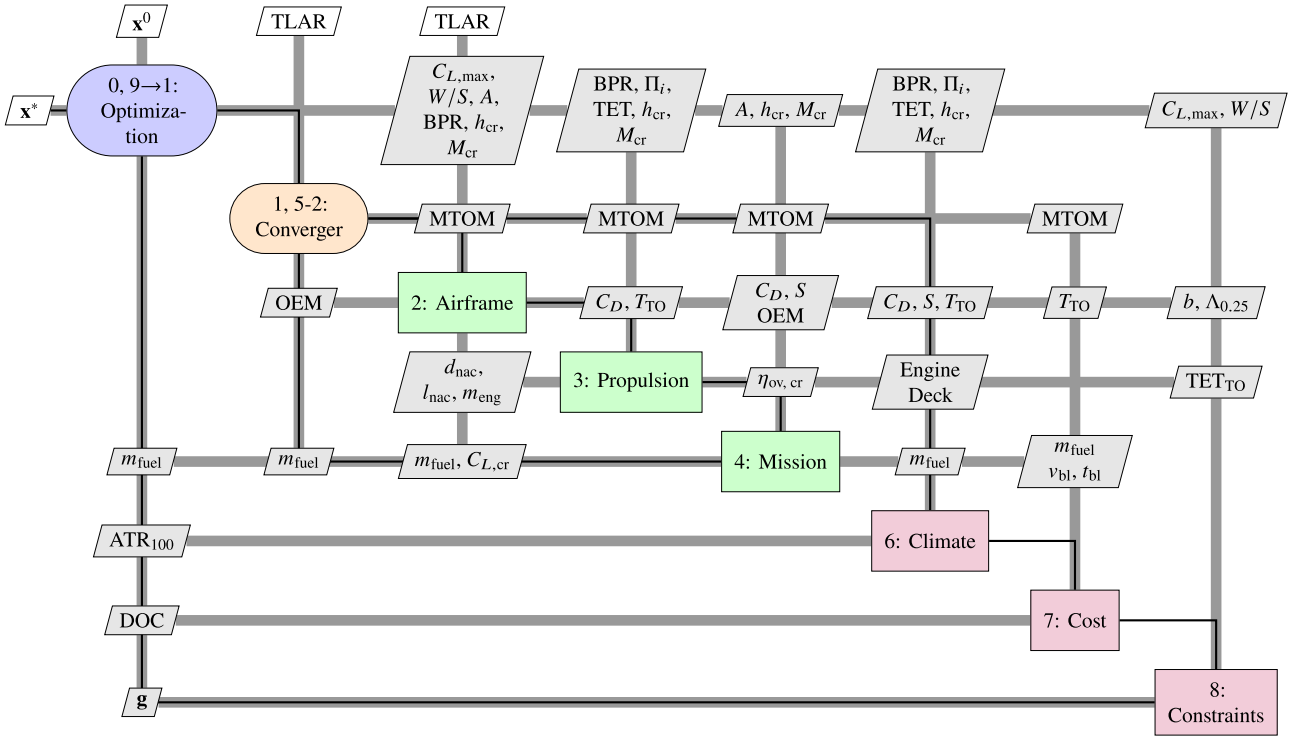

Fig. 2 Extended design structure matrix showing the multidisciplinary design workflow.

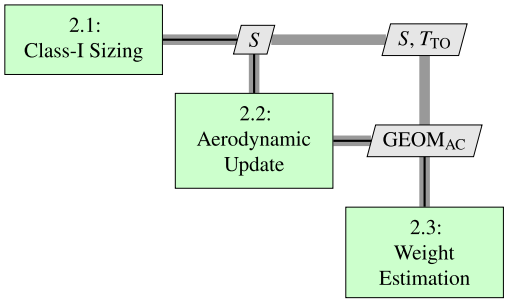

Fig. 3 Airframe design and analysis workflow (step 2 of workflow in Fig. 2).

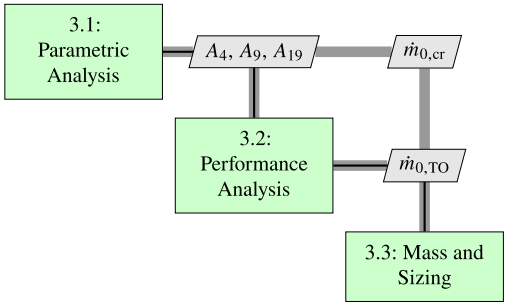

Fig. 4 Propulsion design and analysis workflow (step 3 of workflow in Fig. 2).

$$C_D = C_{D_0} + \beta \cdot C_L^2 \tag{3}$$

for which two constants have to be computed specific to the design variables. The β constant is dependent on the wing aspect ratio A and the Oswald factor e. Obert proposed the following relation to determine β [30], based on statistical analysis:

$$\beta = \frac{1}{\pi A e} \approx \frac{1.05}{\pi A} + 0.007 \tag{4}$$

Table 2 Calculation of temperature, pressure, and density as a function of the selected cruise altitude h_{cr} (in meters) according to the ISA model [$g = 9.81$ m/s^2 and $R = 287$ J/(kg · K)]

Parameter, unit	Troposphere ($0 \le h_{cr} \le 11$ km)	Stratosphere ($11 < h_{cr} \le 20$ km)
Temperature T_{cr}, K	$288.15 - 0.0065 \cdot h_{cr}$	216.65
Pressure p_{cr}, N/m^2	$101325 \cdot (T_{cr}/288.15)^{-g/(0.0065R)}$	$101325 \cdot e^{-g(h_{cr}-11000)/(216.65R)}$
Density ρ_{cr}, kg/m^3	$p_{cr}/(R \cdot T_{cr})$	$p_{cr}/(R \cdot T_{cr})$

The first term of Eq. (3), C_{D_0} (constituting the friction, profile, and excrescence drag), is assumed to be independent of the lift coefficient. C_{D_0} can be calculated by adding the sum of the minimum pressure drag of all aircraft components as well as the drag contributions due to aircraft-size-dependent (control surface gaps, doors, etc.) and aircraft-size-independent (antennas, sensors, etc.) excrescences or protuberances:

$$C_{D_0} = \sum C_{D_{p,\min}} + \Delta C_{D_{E,I}} + \Delta C_{D_{E,II}} \tag{5}$$

The $C_{D_{p,\min}}$ of each component is computed according to the flat-plate analogy, including shape and compressibility corrections. The aircraft-size-dependent excrescence drag $\Delta C_{D_{E,I}}$ is taken to be 1.5% of the total profile drag,

$$\sum C_{D_{p,\min}}$$

assuming hydraulically smooth control surfaces. The size-independent contribution $\Delta C_{D_{E,II}}$ is presumed to be equal to $0.035/S$. To obtain the drag polars in landing and takeoff configurations, constant contributions are added to C_{D_0} and e to account for the extension of the flaps and the landing gear. In the takeoff configuration, contributions of 0.015 and 0.05 [32] are added to C_{D_0} and e, respectively. In the landing phase, C_{D_0} and e are assumed to be approximately 0.085 and 0.10 higher [32] than the nominal values, respectively.

3. Mass Estimation

To capture the effect of design choices on the operating empty mass (OEM) of the aircraft, a class-II weight estimation is implemented. The mass estimation is performed according to the methods presented in appendices C and D of the book by Torenbeek [33]. These semiempirical and statistical methods allow the prediction of the weight of individual structural groups (i.e., wing, fuselage, empennage, undercarriage, and propulsion) as well as the mass of the airframe equipment and operational items.

As can be seen from previous research into global warming impact reduction, the wing aspect ratio is increased in several instances [6,7,10,12] to lower the induced drag. However, this design change can have a dramatic effect on the wing weight, although this penalty may be lessened by increasing the wing thickness and/or decreasing the wing sweep. Although the employed methods are sensitive to the aspect ratio, the result may be inaccurate for high-aspect-ratio values because limited or no reference data are available for such slender wings. Therefore, the aspect ratio is limited to 12.

The structural mass of the fuselage is calculated in a similar manner by employing a combination of statistical and empirical relationships. However, this mass remains (approximately) constant throughout the optimization because the fuselage geometry is independent of the chosen design variables. Because the wing geometry and location affect the geometry of the empennage, the mass of the horizontal and vertical tails is updated throughout the optimizations. This mass prediction is dependent on the respective tail surface and sweep angle. The mass of the undercarriage varies according to the maximum takeoff mass of the aircraft, whereas in all cases, it is assumed that the landing gear is retractable and is located in a low-wing configuration.

As will be further elaborated on in the next section, the mass of the engines is updated according to the required size (i.e., mass flow), bypass ratio, and overall pressure ratio. Also, the impact of high-bypass-ratio engines on nacelle mass is included in the weight assessment of the propulsion group. Furthermore, a forecast of the airframe services and equipment weight is included. The mass of this group is assumed to be equal to a fraction of the maximum takeoff mass (MTOM). This fraction is dependent on the aircraft category. For the operating items, a similar approach is taken.

The outcome of this model is fed forward to the propulsion discipline, the mission analysis, and in the subsequent aircraft iteration to update the wing surface area. Furthermore, to ensure that a consistent mass is adopted in all design modules, the operating empty mass has to converge to complete the convergence loop (Steps 1, 5-2) in the design framework of Fig. 2.

4. Propulsion

In the current aircraft configuration, propulsion is provided by two turbofan engines installed on the wing, which features a two-spool architecture with separate exhausts. Five key design variables are selected for the turbofan cycle: the bypass ratio, the fan pressure ratio Π_{fan}, the low-pressure compressor ratio Π_{lpc}, the pressure ratio of the high-pressure compressor Π_{hpc}, and the total turbine entry temperature. Additional variables required by the discipline are component polytropic efficiencies, mechanical efficiencies, and inlet and combustor pressure losses. These parameters are related to the available technology level and are assumed constant throughout the optimization. Example values of the latter parameters are included in Appendix A for the verification case.

Based on the cruise drag polar and cruise conditions, the thermodynamic cycle is determined by the parametric analysis module of Fig. 4. Subsequently, off-design analysis can be carried out to find the required fuel flow for a given thrust at key points in the mission. Both the on-design and off-design point analyses are executed by employing the strategies laid out by Mattingly et al. [29] and the variable specific heat model introduced by Walsh and Fletcher [34].

Several simplifying assumptions, such as constant component efficiencies, are made in the models to limit computational cost and to eliminate the need for component maps in this early design stage. This loss in accuracy is accepted because the verification cases in Sec. III show limited deviations. Additionally, cooling flows and power extraction are neglected in the current case study for the sake of simplicity.

The results from the thermodynamic analyses are used in the third module of the propulsion workflow in Fig. 4 to estimate the fan diameter and bare engine mass, which are required by the other disciplines to update the aerodynamic drag and structural masses accordingly. The fan diameter is calculated by assuming an axial Mach number of 0.6 at the fan inlet face and a hub-to-tip ratio of 0.3 for the local cross section by taking the spinner into account. The mass of a single turbofan engine is estimated using the following relation [35]:

$$m_{\text{eng}}[\text{lb}] = a \cdot \left(\frac{\dot{m}_{\text{core,TO}}[\text{lb/s}]}{100}\right)^{b} \cdot \left(\frac{\Pi_{\text{core,TO}}}{40}\right)^{c} \tag{6}$$

where a, b, and c are polynomial functions of the bypass ratio. This formulation, which is based on simulations by the more advanced weight estimation software WATE++, allows us to include the weight penalties due to high bypass ratios and pressure ratios, whereas only a limited number of inputs is required.

As briefly introduced in Sec. I, the engine design can have a strong effect on the emitted species. Although high pressure ratios and temperatures typically lead to reduced fuel consumption, and thus low(er) CO_2 emissions, they also increase the production of thermal NO_x [16]. The production of NO_x is also influenced by the detailed combustor design, which is not captured by the current design vector and is out of scope for the current study. From a thermodynamic perspective, the bypass ratio can further improve fuel consumption, although sufficiently high-pressure ratios and temperatures are required to power the large fan [5], worsening NO_x emissions. Finally, increased overall propulsive efficiency due to an increased bypass ratio or OPR is expected to lead to more frequent contrail formation, possibly at higher ambient temperatures [18], and thus at lower altitudes. Hence, balancing the fuel consumption and CO_2 production against the effects of NO_x and contrails is important.

5. Mission Analysis

The aircraft is sized for a standard design mission, for which the mission profile is shown in Fig. 5. Reserve fuel is accounted for by including a diversion range to another airport (approximately 460 km or 250 nm) and a loiter phase of 35 min. In step 4 of the framework presented in Fig. 2, the lost-range method [36] is employed to determine the fuel mass, which is required to iterate upon the MTOM and OEM. This method computes the mission-fuel mass $m_{\text{fuel,mission}}$ to takeoff mass m_{TO} ratio for the standard mission from the cruise range r_{cr}, altitude h_{cr}, lift-to-drag ratio $(L/D)_{\text{cr}}$, and engine overall efficiency $\eta_{\text{ov,cr}}$ according to the following equations:

$$\frac{m_{\text{fuel,mission}}}{m_{\text{TO}}} = \frac{r_{\text{cr}}/R_H}{p + (1/2)\cdot r_{\text{cr}}/R_H} + \frac{h_{\text{cr,eq}}}{0.7\cdot\eta_{\text{ov,cr}}\cdot R_H} + \frac{0.0025}{\eta_{\text{ov,cr}}}$$
$$\text{where } R_H = \frac{\text{LHV}}{g}, \qquad p = \eta_{\text{ov,cr}}\cdot\left(\frac{L}{D}\right)_{\text{cr}}, \qquad h_{\text{cr,eq}} = h_{\text{cr}} + \frac{V_{\text{cr}}^2}{2\cdot g} \tag{7}$$

The three terms in Eq. (7) consider different flight phases: the first term determines the fuel spent during the cruise phase. The second part accounts for the fuel required to takeoff and climb to the cruise altitude, where $h_{\text{cr,eq}}$ combines the altitude increase and the acceleration to cruise speed. The factor $0.7\cdot\eta_{\text{ov,cr}}$ approximates the engine efficiency during the climb phase. The last term adds a minor contribution for maneuvering. Two terms can be included to account for a given diversion range r_{div} and a loiter phase of t_{hold} h [36]:

$$\left(\frac{\Delta m_{\text{fuel}}}{m_{\text{fuel,mission}}}\right)_{\text{div}} = 1.20\cdot\frac{r_{\text{div}}}{r_{\text{harm}}} \tag{8}$$

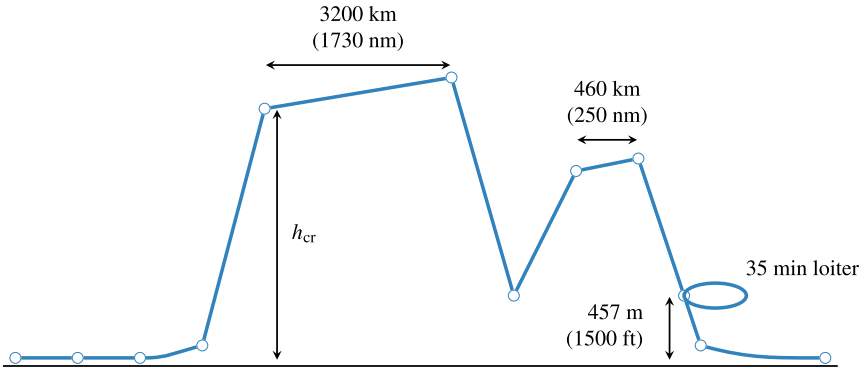

Fig. 5 Mission profile (flown distance versus altitude) under consideration.

$$\left(\frac{\Delta m_{\text{fuel}}}{m_{\text{fuel,mission}}}\right)_{\text{hold}} = 0.20 \cdot t_{\text{hold}} \cdot \frac{R_H}{r_{\text{harm}}} \cdot \left(1 - \frac{m_{\text{fuel,mission}}}{m_{\text{TO}}}\right) \quad (9)$$

In the preceding equations, r_{harm} is the harmonic range of the aircraft. This leads to the following estimate of the total fuel mass required for one trip as a fraction of the takeoff mass:

$$\left(\frac{m_{\text{fuel}}}{m_{\text{TO}}}\right)_{\text{total}} = \frac{m_{\text{fuel,mission}}}{m_{\text{TO}}} \cdot \left[1 + \left(\frac{\Delta m_{\text{fuel}}}{m_{\text{fuel,mission}}}\right)_{\text{div}} + \left(\frac{\Delta m_{\text{fuel}}}{m_{\text{fuel,mission}}}\right)_{\text{hold}}\right] \quad (10)$$

Together with the MTOM estimation from the previous iteration, the required fuel mass can be calculated. This fuel mass is added to the OEM estimation and the payload mass to obtain an updated value for the MTOM. Because this lost-range approach is completely analytical, it can be executed efficiently in the synthesis loop.

However, a more detailed mission analysis is required for the climate impact assessment. This is because the emission index of NO_x depends on the engine pressure ratio, the combustor inlet temperature, and the relative humidity, which vary with the operation conditions. Additionally, the formation of contrails is dependent on the ambient temperature. Also, radiative forcing of these non-CO_2 species is sensitive to the flight altitude.

Therefore, in the climate impact assessment module, the mission is simulated numerically by applying basic flight mechanics rules and by analyzing the engine's off-design performance for discrete time steps. Because this mission assessment approach is more time consuming than the lost-range method, it is only called once in every objective function evaluation rather than in every design iteration.

In the global warming impact evaluation, the accumulated emissions over this design mission and altitude of emission are employed to assess the radiative forcing and the average temperature response. Although this provides insight into the climate burden of the aircraft on this specific mission, it has to be noted that this is not fully representative of an aircraft operated in a more flexible manner in a fleet. Including different missions in the cost and climate assessment is proposed as a recommendation for further research in Sec. V.

6. *Global Warming Impact Evaluation*

As was briefly introduced in Sec. I, the assessment of the climate impact of an aircraft is a nontrivial task. Ideally, the societal costs and damages due to emissions would be calculated and compared to operating costs to make a cost/benefit analysis. However, due to large uncertainties, it is almost impossible to evaluate these costs and damages accurately in a conceptual design stage. Therefore, a suitable climate metric has to be selected. To make an insightful evaluation, Grewe and Dahlmann [37] suggested a five-step process to define the impact valuation and avoid misconceptions.

First, the question to be answered has to be clarified. In this study, the objective is to compare the climate impact of aircraft optimized for different objectives (fuel, costs, and climate impact). Second, the reference aircraft is a nonoptimized yet consistent aircraft design that also serves as a starting point for the optimizations. Third, an emission scenario has to be defined. It has been decided to count the emissions over the entire operational life cycle of a new aircraft to be introduced in 2020. This hypothetical aircraft is assumed to be produced for a period of 30 years, whereas its operational lifetime is assumed to be 35 years (ignoring potential airframe losses). Accordingly, the maximum fleet size will occur in the years of 2050 to 2055. Section IV discusses this fleet scenario definition and productivity constraint in further detail.

Grewe and Dahlmann [37] discussed several climate metrics that are available, as well as their features. In this research, the average temperature response is selected as the metric representing global warming impact because it captures the effect of emissions on the surface temperature change ΔT while limiting the influence of the time horizon on the result. The average temperature response is computed as follows for a period of H years:

$$\text{ATR}_H = \frac{1}{H}\int_0^H \Delta T(t)\,\mathrm{d}t \quad (11)$$

Note that in this section, the time variable t is expressed in years and t_0 represents the initial year of the considered period, e.g., 2020. As a final step of the proposed process, the time horizon H of 100 years is imposed because it provides a balanced assessment between long-lived emissions (CO_2) and more short-lived forcing effects (such as NO_x and contrail formation) [13]. Thus, the final metric is ATR_{100}, which requires the computation of ΔT for each year in the selected time horizon. The temperature change can be computed as follows [14,38]:

$$\Delta T(t) = \int_{t_0}^{t} G_T(t - t') \cdot \text{RF}^*(t')\,\mathrm{d}t' \quad \text{with}$$
$$G_T(t) = \frac{2.246}{36.8} e^{-t/36.8} \quad (12)$$

RF* in Eq. (12) is the normalized radiative forcing (RF). This parameter is equal to one for a doubling in the atmospheric carbon dioxide concentration as compared to preindustrial times. The actual radiative forcing corresponding to a doubling of this concentration, $\text{RF}_{2\times\text{CO}_2}$, is taken to be 3.7 W/m^2 [39]. The normalized radiative forcing in Eq. (12) is the summed value of several species:

$$\text{RF}^*(t) = \sum_{i}^{\text{all species}} \text{RF}^*{}_i(t) = \sum_{i}^{\text{all species}} \left[\text{Eff}_i \cdot \frac{\text{RF}_i(t)}{\text{RF}_{2\times\text{CO}_2}}\right]$$
$$\text{for } i = \text{CO}_2, \text{NO}_x - \text{CH}_4, \text{NO}_x - \text{O}_{3L}, \text{NO}_x - \text{O}_{3S}, \text{H}_2\text{O}, \text{SO}_4, \text{soot, and contrails} \quad (13)$$

Eff_i is the efficacy of a given element, which is equal to the ratio between the climate sensitivity of this species and the climate sensitivity of CO_2 [14]. Table 3 provides values for these efficacy and sensitivity parameters [39–41]. To capture the effects of all these species, a linearized temperature response model is developed

Table 3 Climate sensitivities λ_i and efficacies Eff_i for species under consideration [39–41]

Species	CO_2	CH_4	O_3	H_2O	SO_4	Soot	Contrails
λ_i, K/(W/m^2)	0.73	0.86	1.00	0.83	0.66	0.51	0.43
Eff_i	1.00	1.18	1.37	1.14	0.90	0.70	0.59

(module 6 in Fig. 2), based on methods from the literature. The subsequent paragraphs elaborate on the implemented methods per species that translate the emissions (in kilograms) into the normalized radiative forcing, and subsequently into the approximate temperature change.

a. Carbon Dioxide. The emission of carbon dioxide is directly related to the combustion of fossil fuels, with an emission index of approximately 3.16 kg/kg for kerosene. Carbon dioxide is a greenhouse gas with a long lifetime, which makes the effects independent of the emission location. An increase in the atmospheric concentration of this species results in a warming effect. The methods introduced by Sausen and Schumann [38] provide a convenient approach to estimate the temperature change due to CO_2 emissions. From the emissions in a given year, the change in atmospheric CO_2 concentration, denoted by $\Delta\chi_{CO_2}$, can be computed. This change is given by the following convolution integral:

$$\Delta\chi_{CO_2}(t) = \int_{t_0}^{t} G_{\chi_{CO_2}}(t-t') \cdot E_{CO_2}(t')\,\mathrm{d}t'$$

$$\text{with} \quad G_{\chi_{CO_2}}(t) = \sum_{i=1}^{5} \alpha_i \cdot e^{-t/\tau_i} \tag{14}$$

where E_{CO_2} represents the absolute CO_2 emissions (in kilograms or teragrams) in year t. Table 4 provides the α_i coefficients and perturbation lifetimes τ_i for the impulse response function $G_{\chi_{CO_2}}$. If the concentration change $\Delta\chi_{CO_2}$ is known, the normalized radiative forcing can be obtained from the ratio between the updated concentration and the background concentration $\chi_{CO_2,0}$, which is assumed to be equal to 380 ppmv (parts per million volume):

$$\mathrm{RF}^*(t) = \frac{1}{\ln 2} \cdot \ln\left(\frac{\chi_{CO_2,0} + \Delta\chi_{CO_2}(t)}{\chi_{CO_2,0}}\right) \tag{15}$$

b. Nitrogen Oxides. Although NO_x is not a greenhouse gas itself, it causes several indirect effects that are expected to have a net warming effect [1,42]. However, unlike carbon dioxide, the emission index is not constant but rather dependent on the engine operating condition and combustor technology. There are several options to approximate the emission index, either through an analytical expression [5,7] or through fuel-flow methods [13]. In this research, the analytical expression from Schwartz Dallara [43] is employed:

$$\mathrm{EI}_{NO_x} = 0.0986 \cdot \left(\frac{p_{T3}}{101325}\right)^{0.4} - e^{T_{T3}/194.4 - H_0/53.2} \tag{16}$$

where p_{T3} and T_{T3} are the pressure and temperature ahead of the engine combustor, and H_0 is the specific humidity. This expression can be evaluated at every point in the mission profile from an off-design analysis of the turbofan engine, and it provides the actual emission of NO_x through multiplication with the fuel flow $\dot{m}_{\mathrm{fuel}}$.

Table 4 Coefficients of impulse response function $G_{\chi_{CO_2}}$ in Eq. (14) [38]

	i				
	1	2	3	4	5
α_i	0.067	0.1135	0.152	0.0970	0.041
τ_i	∞	313.8	79.8	18.8	1.7

On a long-term basis, NO_x depletes atmospheric methane (CH_4) and long-lived ozone (O_{3L}), which are both greenhouse gases. The depletion of these agents results in a cooling effect. The radiative forcing of these effects can be modeled according to [41]

$$\mathrm{RF}_i(t,h) = s_i(h) \int_{t_0}^{t} G_i(t-t') \cdot E_{NO_x}(t')\,\mathrm{d}t'$$

$$\text{with} \quad G_i(t) = A_i \cdot e^{-t/\tau_i} \quad \text{for } i = CH_4, O_{3L} \tag{17}$$

In this equation, the coefficient A_i is assumed to be equal to

$$-5.16 \times 10^{-13}\ (\mathrm{W/m^2})/\mathrm{kg}_{NO_x}$$

and

$$-1.21 \times 10^{-13}\ (\mathrm{W/m^2})/\mathrm{kg}_{NO_x}$$

for methane and long-lived ozone, respectively. The perturbation lifetime τ_n is set to 12 years. Note that $s_i(h)$ is a forcing factor, as defined in Ref. [41], to account for the altitude variation of NO_x and contrail effects.

The most prominent warming effect of NO_x emissions is the formation of short-lived ozone in the troposphere and lower stratosphere. Because this is a short-lived effect, no convolution integral with response function is required, but a simpler method can be applied:

$$\mathrm{RF}_{NO_x-O_{3S}}(t,h) = s_{NO_x-O_{3S}}(h) \cdot \left(\frac{\mathrm{RF}_{\mathrm{ref}}}{E_{\mathrm{ref}}}\right)_{NO_x-O_{3S}} \cdot E_{NO_x}(t) \tag{18}$$

Similar to Eq. (17), a forcing factor $s(h)$ is also included here to simulate the altitude dependency of the radiative effects. The constant $\mathrm{RF}_{\mathrm{ref}}/E_{\mathrm{ref}}$ represents the radiative forcing due to $NO_x - O_{3S}$ per unit of NO_x emission. It is assumed to be equal to

$$1.01 \times 10^{-11}\ (\mathrm{W/m^2})/\mathrm{kg}_{NO_x}$$

although a large uncertainty is present.

This assessment of NO_x depends on certain simplifying assumptions. First, the changing lifetime of methane, due to its depletion, is not taken into account [44]. This can be considered a steady-state assumption. Finally, although also the geographic location of emissions performs a role, it is not taken into account in this analysis.

c. Water, Soot, and Sulfate. In the combustion process, other short-lived species are also formed, such as water vapor and aerosols such as soot (black carbon) and sulfate. To compute the absolute emissions of these species, constant emission indices (EIs) are assumed: $\mathrm{EI}_{H_2O} = 1.26$ kg/kg, $\mathrm{EI}_{\mathrm{soot}} = 2.0 \times 10^{-4}$ kg/kg, and $\mathrm{EI}_{SO_4} = 4.0 \times 10^{-5}$ kg/kg [41]. The impact of these species is modeled in a similar manner to the short-lived ozone production discussed earlier in this paper. However, for these species, the altitude dependency factor is omitted, resulting in the following relation [41]:

$$\mathrm{RF}_i(t) = \left(\frac{\mathrm{RF}_{\mathrm{ref}}}{E_{\mathrm{ref}}}\right)_i \cdot E_i(t) \quad \text{for } i = \mathrm{soot}, H_2O, SO_4 \tag{19}$$

d. Contrails. Because the jet exhaust of the turbofan engines is hot and humid as compared to the ambient air, condensation trails may form behind an aircraft. Whether or not contrails indeed develop can be assessed with the help of the Schmidt–Appleman criterion [18]. This criterion is met if the hot exhaust air reaches saturation with respect to liquid water during the mixing process with the surrounding air. The mixing process is modeled by a mixing line in a diagram of water vapor partial pressure versus ambient temperature. This

mixing line can be approximated by a linear relationship that depends on the ambient conditions (pressure, temperature, and relative humidity), the overall engine efficiency, and the emission index of water.

Additionally, the formation can only occur when the static ambient temperature lies below the temperature threshold of 235 K (−38°C). These conditions are not sufficient to ensure that the contrails are persistent. For this to occur, the partial pressure of the mixed exhaust, which has reached the ambient temperature, should lie in between the thresholds for saturation above liquid water and the saturation level above ice. The formulas provided by Sonntag [45] specify these levels as a function of temperature.

These three criteria are evaluated at every point in the mission analysis by using the International Standard Atmosphere model to obtain the ambient conditions. The selected cruise altitude and engine design variables are expected to influence the outcome. If all three criteria are met, then that point is marked as a time interval in which persistent contrails appear. At the end of the mission analysis, the total contrail length (in kilometers or nautical miles) is used to estimate the radiative forcing according to [41]

$$\mathrm{RF}_{\mathrm{contrails}}(t,h) = s_{\mathrm{contrails}}(h) \cdot \left(\frac{\mathrm{RF}_{\mathrm{ref}}}{L_{\mathrm{ref}}}\right)_{\mathrm{contrails}} \cdot L(t) \tag{20}$$

where $s_{\mathrm{contrails}}(h)$ is an altitude-dependent forcing factor,

$$\left(\frac{\mathrm{RF}_{\mathrm{ref}}}{L_{\mathrm{ref}}}\right)_{\mathrm{contrails}}$$

is set to 1.82×10^{-12} $(\mathrm{W/m^2})/\mathrm{km}$ [2], and $L(t)$ is the accumulated contrail length in year t.

It has to be recognized that the contrail assessment method presented in this section is simplified and that uncertainties remain. Although the results are sensitive to changes in flight altitude and technology variables, the fact that atmospheric conditions may vary regionally or temporally is not accounted for. Additionally, the dependency of the radiative effects on the geographic location is neglected. Finally, only the impact of linear contrails is analyzed. The formation and effects of contrail cirrus are not considered.

7. *Operating Costs*

Although the fuel costs constitute a large portion of an aircraft's operating costs, other contributions play an important role as well. Reducing the block time t_{bl} by increasing the flight speed, for example, decreases the crew costs but may lead to higher fuel costs. Module 7 of Fig. 2 employs the methods presented by Roskam ([46] chap. 5) to estimate the cash operating costs for a particular aircraft design [in U.S. dollars (USDs) per seat per nautical mile or USDs per seat per kilometer] or for a complete fleet (in USDs).

Two main contributions are included in the analysis. First, the costs related to flight itself are estimated. These comprise fuel and oil costs, crew salaries, and insurance. A fuel price of 1.78 USDs/U.S. gallon is assumed, which is approximately equal to the price level in January 2020 before the influence of the Corona pandemic. The following relation determines the fuel and oil costs per seat per nautical mile:

$$C_{\mathrm{fuel}} = \frac{m_{f,\mathrm{bl}}}{r_{\mathrm{bl}} \cdot N_{\mathrm{pax}}} \cdot \frac{C_{f,\mathrm{gal}}}{\rho_{\mathrm{fuel}}} \tag{21}$$

$$C_{\mathrm{oil}} = \frac{m_{\mathrm{oil}}}{r_{\mathrm{bl}} \cdot N_{\mathrm{pax}}} \cdot \frac{C_{\mathrm{oil,gal}}}{\rho_{\mathrm{oil}}} = \frac{0.7 \cdot N_{\mathrm{eng}} \cdot t_{\mathrm{bl}}}{r_{\mathrm{bl}} \cdot N_{\mathrm{pax}}} \cdot \frac{C_{\mathrm{oil,gal}}}{\rho_{\mathrm{oil}}} \tag{22}$$

The captain, first officer, and flight attendant salaries are also adapted to 2020 levels. It is assumed that each crew member flies 1000 h annually and that at least one cabin crew member is present for each 50 passengers. The cost of a single crew member, expressed in USDs per seat per nanometer, is defined as follows [46]:

$$C_{\mathrm{crew\,member}} = \frac{1}{N_{\mathrm{pax}} \cdot V_{\mathrm{bl}}} \cdot \left[(1 + k_j) \cdot \frac{\mathrm{sal}_{\mathrm{crew\,member}}}{\mathrm{ah}_{\mathrm{crew\,member}}} + t_{\mathrm{ef}}\right] \tag{23}$$

Table 5 Parameters related to the cost estimation of the flight crew

Parameter, unit	Symbol	Value
Factor for employer costs	k_j	0.26 [46]
Annual captain salary, USDs/year	$\mathrm{sal}_{\mathrm{captain}}$	277,000[a]
Annual first officer salary, USDs/year	$\mathrm{sal}_{\mathrm{first\ officer}}$	188,000[a]
Annual cabin crew member salary, USDs/year	$\mathrm{sal}_{\mathrm{cabin\ crew}}$	43,160[b]
Annual flight hours, h/year	ah	1000[a]
Travel expense factor, USDs/h	t_{ef}	9 [46]

[a]Data available online at https://epicflightacademy.com/airline-pilot-salary/ [retrieved 24 November 2020].
[b]Data available online at https://www.indeed.com/cmp/American-Airlines/salaries/Flight-Attendant [retrieved 24 November 2020].

The parameters in the preceding equation are explained and quantified in Table 5. The annual hull insurance rate (in USDs per USDs per airplane per year) is taken to be 0.02.

Second, the cost of maintenance $C_{\mathrm{maintenance}}$ is accounted for through the methods introduced in section 5.2.2 of Ref. [46]. This category includes the labor rates of the airframe and engine engineers (2020 averaged salaries), as well the cost for airframe and engine spares. The latter two aspects require an appreciation of the aircraft and turbofan engine unit purchase prices. New relations are derived to estimate these prices, based on the aircraft OEM and the single engine static takeoff thrust, from recent price figures[§,¶]:

$$P_{\mathrm{AC},2020}[2020\,\mathrm{USD}] = 0.0052 \cdot \mathrm{OEM}^{0.927} \cdot 10^6 \tag{24}$$

$$P_{\mathrm{eng},2020}[2020\,\mathrm{USD}] = 0.1604 \cdot T_{\mathrm{TO,eng}}^{0.878} \cdot 10^6 \tag{25}$$

The values of the OEM and $T_{\mathrm{TO,eng}}$ in these relations are expressed in kilograms and kilonewtons, respectively. Other cost contributions, such as depreciation and fees related to financing and operations, are excluded from the analysis. The reason for this exclusion is that these categories are thought to carry more uncertainty and that they may be dependent on business decisions. For example, the financing cost may depend on the decision of whether to buy or lease the aircraft. Additionally, indirect operating costs (such as passenger services, station operation, promotion, and administration) are neglected in the current analysis.

In module 7 of Fig. 2, first, the direct operating costs of one aircraft are calculated. However, because the climate impact is determined for an operating fleet, for a prolonged period of time, it is of interest to express the costs in a similar manner. Knowing the operating cost of one aircraft per year $C_{\mathrm{ops,AC}}$, the total fleet operating costs $C_{\mathrm{ops,fleet}}$ can be computed as follows:

$$C_{\mathrm{ops,fleet}} = C_{\mathrm{ops,AC}} \cdot \mathrm{RPK}_{\mathrm{AC,ann}} \cdot N_{\mathrm{yr}} \cdot N_{\mathrm{AC}} \tag{26}$$

$$= (C_{\mathrm{fuel}} + C_{\mathrm{oil}} + C_{\mathrm{crew}} + C_{\mathrm{insurance}} + C_{\mathrm{maintenance}}) \cdot \mathrm{RPK}_{\mathrm{AC,ann}} \cdot N_{\mathrm{yr}} \cdot N_{\mathrm{AC}} \tag{27}$$

where $\mathrm{RPK}_{\mathrm{AC,ann}}$ is the amount of revenue passenger kilometers flown by one aircraft in one year, N_{yr} is the operational life of an aircraft, and N_{AC} is the total number of aircraft in the fleet. Values for the latter parameters may vary between objectives due to a difference in block time, and thus productivity. Section IV.A discusses this aspect in further detail and introduces the hypothetical fleet scenario.

[§]"2018 Price Adjustment Across Airbus' Modern Product Range Reflects Continuous Investment and Customer Value," Airbus Media Relations, 2018, https://www.airbus.com/sites/g/files/jlcbta136/files/2021-07/new-airbus-list-prices-2018.pdf [retrieved 2 September 2020].

[¶]"About Boeing Commercial Airplanes," The Boeing Company, Chicago, IL, 2020, http://www.boeing.com/company/about-bca/ [retrieved 2 September 2020].

III. Verification of Analysis Methods

This section verifies whether the methods described earlier in this paper work correctly, as well as whether the overall methodology results in a realistic case study. Special attention is paid to the physics-based propulsion discipline in Sec. III.A because an accurate estimation of the engine parameters is required to predict the emissions in the climate impact evaluation module. In Sec. III.B, two aircraft are designed for the same top-level requirements as the Airbus A320-200 and Boeing 777-200 to confirm that the implemented approach allows production of a realistic conceptual aircraft design.

A. Turbofan Performance Verification

The verification of the propulsion discipline consists of two steps: first, the design and off-design analyses produced by the implemented methods are compared to a model of the GE90 in the Gas turbine Simulation Program (GSP) gas turbine simulation program. Second, a performance map for varying Mach numbers and altitudes is constructed and compared to GE90 performance data provided by Nicolai and Carichner [47]. The inputs employed to model the GE90 engine are provided in Appendix A. Table 6 presents the results of the first verification step. The subscripts indicate the engine stations according to the international standard ARP 755A station numbering standard. Although both the implemented method and the GSP model employ the same inputs, the GSP model also includes component maps that provide component efficiency updates according to the operating condition. It can be concluded that the errors between the two models are relatively small and that simplified methods provide sufficient accuracy. A study of the errors in the design point analysis indicates that these can be attributed to minor differences in the variable specific heat models.

Second, an engine deck of the GE90 is created and compared to data provided in appendix J of the work of Nicolai and Carichner [47]. The results are presented in Figs. 6 and 7 for the net thrust and fuel flow. The values are normalized with respect to the sea-level-static (SLS) values because absolute differences may occur because it is unclear for which exact GE90 type the data are provided. From these figures, it can be observed that the thrust and fuel-flow values correspond rather well for varying altitudes and Mach numbers when considering the simplifying assumptions discussed earlier in this paper.

B. Aircraft Synthesis Verification

This section discusses the validity of the aircraft design methods and synthesis loop introduced in Sec. II. The comparison between existing aircraft data and the simulated models is based on three aspects: the mass estimation, the geometry creation, and performance evaluation. These aspects are considered for two aircraft, namely, the Airbus A320-200 and the Boeing 777-200, representing the narrow-body and wide-body categories. Input values for these two aircraft are included in Appendix B.

First, Table 7 presents the mass estimation obtained with the framework and compares four key geometric dimensions for both aircraft [48]. These results are obtained after six iterations in the inner convergence loop of the methodology (Fig. 2). The relative differences for these parameters lie between to −1.6 and +2.5%, which is considered acceptable when given the conceptual design level and the simplifying assumptions made in the methodology.

Second, Fig. 8 shows the resulting geometry predictions and the overlap with the actual top view of the aircraft [49,50]. Although the computational models agree relatively well with the actual planform, two aspects can potentially be further improved. First, the wing taper ratio is overestimated for both cases. This is because the statistical relation, which relates the taper ratio to the wing sweep, produces an averaged value for various aircraft. For example, it underestimates the taper for a Boeing 737-700. Therefore, it is decided to not correct this relation for the aircraft presented here. Also, the main wing of the Airbus A320-200 is placed slightly more aft than expected. Again, this can be attributed to averaged statistical values: in this case, the location of the aircraft center of gravity (c.g.) at the OEM with respect to the mean aerodynamic chord (MAC; $\xi_{cg,OEM} = 0.25MAC$), and the relative location of the horizontal tail to the fuselage length

Table 6 Verification of the performance analysis with the implemented methods versus GSP (conditions according to Table A1; bold numbers represent input values)

	Design (cruise)			Off-design (takeoff)		
Parameter, unit	Framework	GSP	Difference, %	Framework	GSP	Difference, %
T_{T3}, K	772	771	+0.09	896	897	−0.13
p_{T3}, Pa	1.42	1.42	+0.04	3.46	3.47	−0.37
T_{T4}, 10^3 K	**1.43**	**1.43**	**0**	1.65	1.66	−0.69
p_{T4}, Pa	1.35	1.35	+0.04	3.29	3.30	−0.38
$\dot{m}_0$, 10^3 kg/s	0.557	0.558	−0.17	1.30	1.29	+0.45
$\dot{m}_{fuel}$, kg/s	1.16	1.14	+1.37	3.10	3.10	−0.05
TSFC, kg/(N · s)	1.49×10^{-5}	1.46×10^{-5}	+1.75	8.22×10^{-6}	8.22×10^{-6}	−0.05
N1, %	**100**	**100**	**0**	106	103	+3.12
N2, %	**100**	**100**	**0**	107	106	+0.86

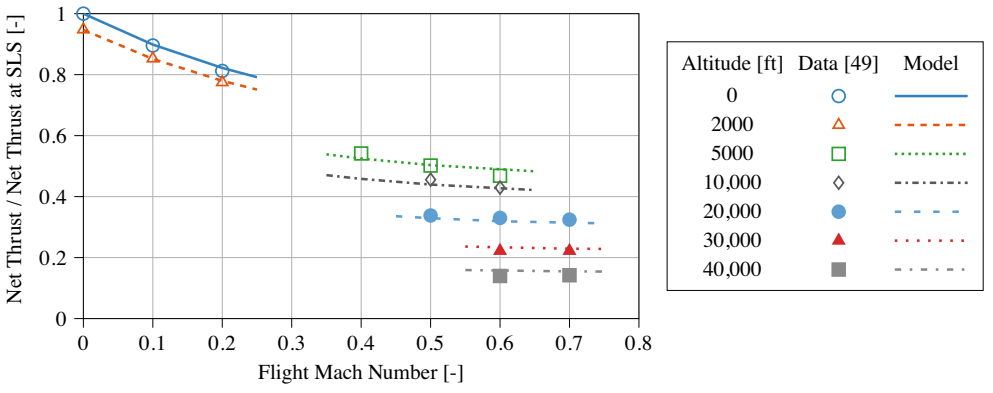

Fig. 6 Validation of maximum net thrust calculation throughout the flight envelope as compared to GE90 engine data (Ref. [47] appendix J).

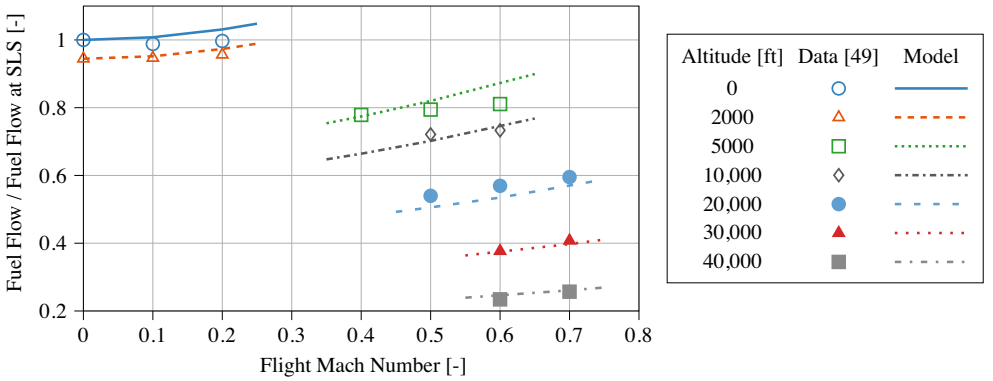

Fig. 7 Validation of fuel-mass flow at maximum net thrust calculation throughout the flight envelope as compared to GE90 engine data (Ref. [47] appendix J).

Table 7 Validation of aircraft design modules with Airbus A320-200 and 777-200 [48] (fuel mass is evaluated at harmonic range with maximum structural payload)

	Airbus A320-200			Boeing 777-200		
Parameter, unit	Framework	Reference	Difference, %	Framework	Reference	Difference, %
MTOM, tons	72.3	73.5	−1.6	242	243	−0.5
OEM, tons	40.7	41.3	−1.5	134	136	−1.4
Fuel mass, tons	13.3	13.5	−1.2	52.3	52.2	+0.3
Wing area S, m^2	126	122	+2.5	437	428	+2.1
Wingspan b, m	34.5	34.1	+1.3	61.6	60.9	+1.2
Fuselage outer diameter d_{fus}, m	3.96	3.95	+0.2	6.14	6.20	−1.0
Fuselage length l_{fus}, m	38.2	37.6	+1.8	62.6	62.8	−0.3

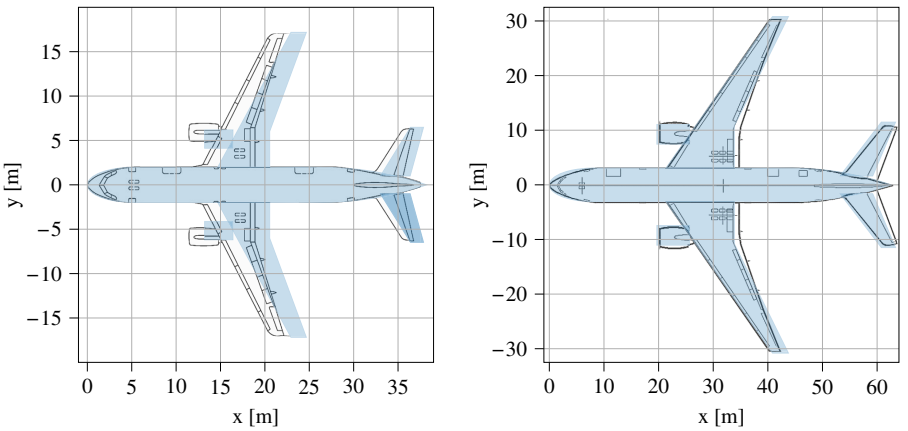

a) Airbus A320-200 **b) Boeing 777-200**

Fig. 8 Comparison between the top view created by the Multidisciplinary design optimization (MDO) framework (light blue) and the actual geometry (dark lines) [49,50].

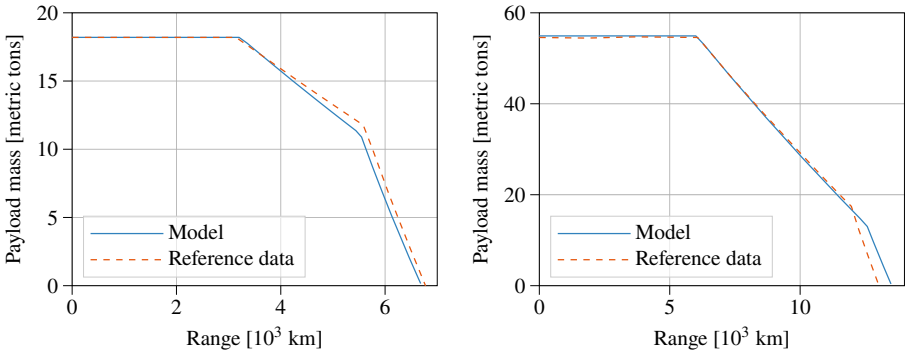

a) Airbus A320-200 (M_{cr}=0.78, h_{cr}=11.3 km) **b) Boeing 777-200 (M_{cr}=0.84, h_{cr}=11.9 km)**

Fig. 9 Comparison between payload/range diagrams obtained with the MDO framework (blue lines) and the reference diagrams (dashed orange lines) [49,50].

($x_{ht}/l_{fus} = 0.91$). The geometry creation is discussed more elaborately in Appendix C.

Finally, to verify whether the aircraft performance is evaluated adequately, the payload/range diagrams of the aircraft are compared in Fig. 9 with data from aircraft characteristics documents. Also, for the performance aspect, good agreement is achieved with the relatively simple methodology. For the Airbus A320, the slope of the line between the harmonic mission and full fuel tanks is marginally underestimated, which is possibly caused by an underestimation of the engine efficiency or the lift-to-drag ratio in the cruise segment. This approximation of this slope is better for the Boeing 777, although the range at maximum fuel capacity is somewhat overestimated.

IV. Results

Employing the verified methodology from Sec. II, a commercial aircraft design is optimized for a given set of top-level requirements. This section presents the results of a series of optimizations and discusses the rationale behind the design results. We carried out optimizations for the three objectives of climate impact ATR_{100}, fleetwide fuel mass $m_{fuel,fleet}$, and operating costs $C_{ops,fleet}$ by varying the 10 design variables introduced in Table 1. Table 8 presents the top-level requirements that are used throughout all optimization studies. These requirements correspond to a narrow-body, medium-range aircraft, which is comparable to the Airbus A320 or Boeing 737. The specified structural payload represents a high-density cabin layout of 180 passengers in economy class seats, resulting in a maximum structural payload of approximately 18 tons.

Because previous studies [7,13] revealed that climate-optimized aircraft tend to fly slower, with an increased block time as the result, it is of interest to study whether such an aircraft can maintain the same productivity level. To gain further insight into this matter, the hypothetical fleet scenario includes a productivity constraint, as introduced in Sec. IV.A. Subsequently, Sec. IV.B presents the optimization results. The optimization strategy is elaborated upon separately in Appendix D.

A. Future Fleet Scenario Definition

Because the climate impact is calculated from an emission scenario of over 100 years, the outcome is dependent on the number of flights taking place in this period, and thus the number of active aircraft. Assuming all aircraft in the hypothetical fleet execute only one fixed mission, the number of flights in a given year (year i) is computed from the number of aircraft available in that year, the block time t_{bl} of that mission, and the annual utilization U_{ann} of the aircraft type:

$$N_{\text{flights,year } i} = N_{\text{AC,year } i} \cdot \frac{U_{ann}}{t_{bl}} \tag{28}$$

We assume a constant annual utilization, which is equal to 3700 h per year for the narrow-body aircraft category studied here. This value follows from statistical analysis of 15 U.S.-based airlines from 1995 to 2019 [51]. The chosen mission largely determines the block time. In this research, the three objectives are evaluated for a fixed mission with $N_{pax} = 130$ passengers (i.e., 13 tons of payload) and a stage length r_{bl} of 1852 km or 1000 nm. Research by Husemann et al. [52] indicates that narrow-body aircraft often operate near this payload/range combination.

Table 8 Top-level aircraft requirements employed for the aircraft optimization

Requirement, unit	Value
Maximum structural payload, tons	18.2
Harmonic range, km (nm)	3200 (1730)
Approach speed, m/s (kt)	70.0 (136)
Takeoff length (ISA conditions), m (ft)	2100 (6890)

Additionally, the block time varies with the cruise speed, and is thus different for the three objectives, as shown in the subsequent section. Because the varying block time affects the productivity of an aircraft (i.e., the number of passenger kilometers flown in a given timeframe), the number of aircraft is not constant, but rather the required productivity in the year 2050 is kept constant. This productivity level is equal for all three objectives under consideration. The imposed level is estimated from passenger transport statistics in the United States for 15 airlines [51] by considering an annual growth of 3% in this region [3]. Hence, this aircraft fleet has to reach a productivity level of approximately 3.95×10^{12} revenue passenger kilometers $RPK_{fleet,2050}$ each year in the period from 2050 to 2055.

By imposing this constraint, the total number of flights carried out each year is also equal for the three objectives. In this case, the maximum number of aircraft to be produced, as well as the number of aircraft active in the period from 2050 to 2055, is provided by the following relation:

$$N_{AC,2050} = \frac{RPK_{fleet,2050}}{N_{pax} \cdot r_{bl}} \cdot \frac{t_{bl}}{U_{ann}} = \frac{3.95 \cdot 10^{12}}{130 \cdot 1852} \cdot \frac{t_{bl}}{3700} \tag{29}$$

The production of the new, hypothetical aircraft starts in 2020, and it continues for 30 years. Each aircraft has a lifetime of 35 years, assuming no hull losses occur. The aircraft concept is thus in operation for a period of 65 years. Figure 10 clarifies the scenario construction by presenting the total fleet size and the number of flights for each year in the period of 100 years considered for the climate impact evaluation. The following section discusses the differences between the objectives.

B. Single-Objective Optimization Results

Table 9 presents the results of the optimizations for the three objectives introduced at the start of this section. On the left-hand side of the table, the absolute values of the parameters are provided for each optimized objective. The right-hand side shows the relative

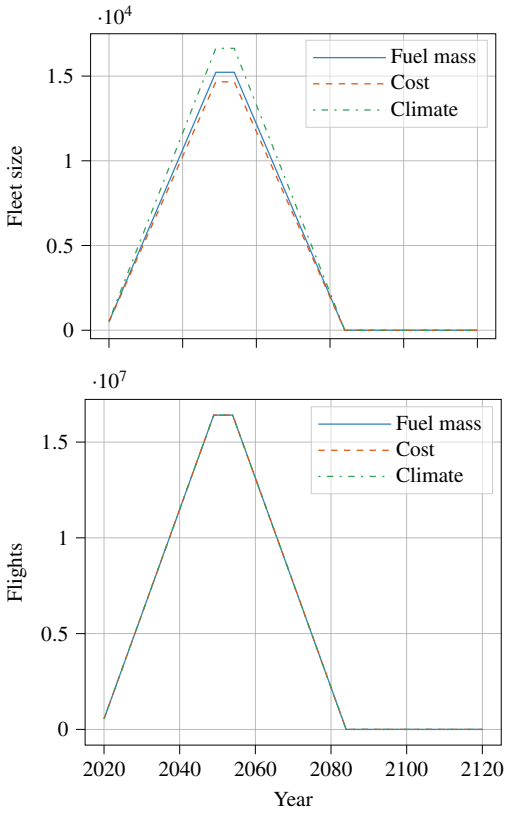

Fig. 10 Future amounts of aircraft in operation and number of flights in the hypothetical scenario.

Table 9 Optimized objective values (denoted by *) and relative differences

	Absolute values			Relative to minimum value		
Objective	m_{fuel}, 10^{11} kg	C_{ops}, 10^{13} USD	ATR_{100}, mK	m_{fuel}, %	C_{ops}, %	ATR_{100}, %
Fuel mass	1.19*	9.87	26.8	— —	+2.6	+128
Cost	1.26	9.62*	27.0	+6.1	— —	+130
Climate	1.27	10.4	11.8*	+6.6	+8.2	— —

changes with respect to the minimum achievable value. For example, when an aircraft is optimized for ATR_{100}, the operating costs lie 8.2% above the minimum cost achievable, and the fuel burn is 6.6% higher than the minimum fuel mass found.

The results indicate that none of the three objectives leads to the exact same solution. Although the fuel- and cost-optimized aircraft are rather similar, they appear to be conflicting with the global warming objective. Indeed, even by combining airframe, engine, and mission variables, it seems that the climate-optimized solution does not correspond to the minimum fuel burn solution and that operating costs are increased. Tables 10 and 11 show the selected design variables and other performance indicators, respectively, to shed a light on the design choices made for each individual design objective. The resulting top views of the optimized aircraft are displayed in Fig. 11.

In the case of the fuel-mass objective, it is clear that the optimizer moves to a design point with a high aspect ratio for reduced lift-induced drag. Furthermore, the overall pressure ratio of 56.7 approaches the highest value allowed within the specified bounds. The bypass ratio of 9.0 is relatively high but not maximized. This may be due to a tradeoff with installation effects, and because the allowable turbine entry temperature in takeoff conditions is limited. These design changes result in an optimal fuel consumption of approximately 5200 kg per flight.

Table 10 Optimized design variables for the three design objectives considered

Variable, unit	Fuel mass	COC	ATR_{100}
W/S, kN/m^2	6.03	5.55	6.08
A	11.6	9.05	12.0
$C_{L_{max}}$	2.69	2.60	2.80
BPR	9.00	7.12	10.5
Π_{fan}	1.59	1.80	1.40
Π_{lpc}	1.80	1.42	1.37
Π_{hpc}	19.8	20.0	19.5
TET, 10^3 K	1.52	1.55	1.45
h_{cr}, km	10.1	10.2	7.56
M_{cr}	0.708	0.751	0.600

Table 11 Performance indicators of optimized aircraft

Parameter	Fuel mass	COC	ATR_{100}
MTOM, tons	68.5	68.2	66.9
OEM, tons	38.5	37.4	36.0
S, m^2	111	121	108
$\Lambda_{0.25}$, deg	16.3	22.0	0.0
λ	0.325	0.277	0.460
$(L/D)_{cr}$	19.3	18.2	18.8
$(T/W)_{TO}$	0.329	0.315	0.317
T_{TO}, kN	221	211	207
$TSFC_{cr}$, kg/(N · s)	1.51	1.61	1.47
t_{bl}, h	3.62	3.49	3.95
$N_{AC,max}$	15,226	14,663	16,637

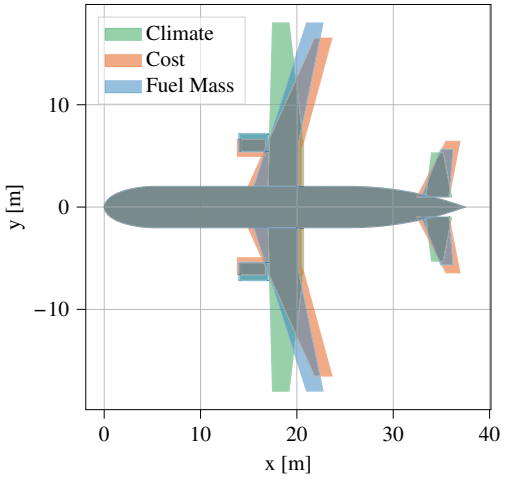

Fig. 11 Top view of aircraft optimized for three different objectives.

The design of the aircraft with minimized operating costs [approximately 0.129 USD_{2020}/(seat · nm)] appears to be driven by the block time, which is the shortest of the optimized aircraft, as can be seen in Table 11. This parameter and its related block speed play important roles in the labor costs of the crew and maintenance technicians because these costs are related to the flight hours. Although the fuel costs perform an important role in cost minimization, they are not dominant. Nevertheless, the relative contribution depends on the fuel price, which is assumed to be 1.78 USD/U.S. gallon in this study. Higher fuel prices for given labor rates can make the design more sensitive to the fuel burn. Ideally, the aircraft would fly at an even higher Mach number to reduce labor costs further. Nonetheless, this is hindered by the constraint on the maximum lift coefficient, which decreases with increased sweep, and thus cruise speed.

Additionally, because this $C_{L,max}$ constraint appears to be active for all objectives, the variable can be removed from the design vector in future optimization studies with the current framework. Rather, $C_{L,max}$ can be calculated directly from the quarter-chord sweep angle, which in turn follows from the selected cruise Mach number.

The climate-optimized aircraft, however, exhibits a different design. The average temperature response also takes the short-lived climate agents into account, of which NO_x and contrails are prevalent and have an altitude dependency. It can be seen in Table 10 that the optimal cruise altitude is considerably lower than the fuel-optimized and cost-optimized aircraft, i.e., 7.56 km vs 10.1 km. This can be explained as follows: in the case of NO_x, this reduces the radiative forcing due to the creation of short-lived ozone [53]. For contrails, flying lower reduces the probability of contrail formation due to the higher ambient temperatures. These two effects are reinforced by the choice of engine design variables: the lower design OPR (37.4 compared to 56.7 for the fuel-mass objective) reduces the emission index of NO_x and decreases the overall engine efficiency (29.5% compared to 32.7% for the fuel-mass objective). The latter aspect reduces the slope of the mixing line in the Schmidt–Appleman criterion, lowering the probability of persistent contrail formation further. It can be argued that this also reduces the climate impact due to contrail cirrus, although this is not considered in the optimizations.

Furthermore, it is observed that the aircraft operates at a significantly lower Mach number of 0.60 at the lower bound of this variable.

It is expected that two reasons lead to this result: first, the cruise speed has to be adapted to the lower altitude to achieve the optimal lift-to-drag ratio in cruise. Second, the lower Mach number does not require a (large) sweep angle and allows for larger thickness-to-chord ratios, with both reducing the structural mass of the wing. To better suit the operation at such low Mach numbers, it would of interest to study exchanging the turbofan cycle for a propeller-based propulsion system.

Although the engine efficiency of the climate-optimized aircraft is reduced, the data in Table 11 indicate that the thrust specific fuel consumption (TSFC) is slightly lower as compared to the fuel- and cost-optimized aircraft. This may appear to be contradictory. Nevertheless, it is correct that the efficiency of the climate-optimized aircraft is lower: not only due to the decrease in overall pressure ratio but also because of the lower cruise speed. The latter design choice simultaneously lowers ram pressure and ram drag, which causes a beneficial reduction in TSFC and a decrease in the propulsive efficiency of the turbofan engine. These opposing trends of the TSFC and propulsive efficiency with respect to flight speed were also documented by Torenbeek (Ref. [33] chap. 4).

The temperature response over the next 100 years is presented in Fig. 12 for the three objectives. The difference in the climate impact of the three aircraft becomes apparent in this figure because the ATR_{100} objective is related to the area under these curves. The line corresponding to the fuel-mass objective shows a relatively high maximum in 2075 because the short-term climate effects are prevailing, whereas the impact of long-lived CO_2 emissions (which relate linearly to fuel consumption) is reduced. For the climate-optimized case, the short-term effects are minimized, but the maximum occurs later due to the delayed effect of CO_2 emissions.

Additionally, upon further examination of Fig. 12, the surface temperature change in the year 2120 approaches approximately 20–25 mK for all cases. Hence, one may argue that the final effect is the same. Nevertheless, the climate-optimized airplane does not reach the same level of temperature change around 2075. This is captured by the ATR_{100} metric and shows that this metric can give insight into global warming by capturing short- and long-term effects of several species.

A final remark on the fixed productivity approach is that approximately 13% more aircraft have to be produced in the case of the climate-optimized aircraft, at a higher production rate, to reach the same productivity level in the period from 2050 to 2055. This is indicated in Fig. 10. The need for more aircraft is a consequence of the higher block time, which reduces the productivity of a single aircraft. To maintain the same level of fleet productivity, more aircraft of this type have to be operated. Neither the climate impact nor the costs of this larger production capacity are computed in this research. However, one could argue qualitatively that this increased production raises both the climate footprint and the complete life-cycle cost of the climate-optimized aircraft.

During the operational lifetime of this aircraft, from 2020 to 2085, the technology levels will likely evolve and affect the propulsion, aerodynamic, and structural disciplines. This study does not quantify the impact of such developments on the optimized aircraft. Nevertheless, a qualitative outlook is provided here. Because a single aircraft type is considered with a market introduction in 2020, the airframe will remain almost constant throughout the considered lifespan, albeit with minor aerodynamic and structural improvements. These improvements can enhance the cruise efficiency, leading to lower fuel burn and reduced absolute emissions. Although the aircraft mass alters contrail properties [54], the effect is mainly dependent on aircraft category and is difficult to quantify in the conceptual phase. An engine upgrade during the aircraft's lifetime is feasible, which can drastically influence the overall fuel burn and emissions through improved component efficiencies and combustor design. Producing less NO_x emissions at higher overall pressure ratios would be beneficial, and it could increase the optimal cruise altitude and Mach number. A study with updated design assumptions (such as increased aspect ratio, bypass ratio, and temperature bounds) is recommended to reflect on future technology levels by considering a later entry into the market. Next to the aerodynamic and possible efficiency benefits, the effect of such technologies on other disciplines such as mass should also be properly taken into account in the methods.

C. Multiobjective Optimization Results

This section describes the results of multiobjective optimization to study the tradeoff between climate impact and operating costs. The Pareto front defining this tradeoff is presented in Fig. 13. This image shows that for a marginal cash-operating cost increase of 1 to 2%, a significant reduction in ATR_{100} is already possible. This large reduction potential comes mostly from the reduction in cruise altitude and Mach number. Although uncertainties remain, it seems that to significantly lower the climate impact while limiting the cost increase, a design solution near a 50% ATR_{100} reduction and a 2% cost increase is preferred over the climate-optimal solution. Beyond this point, the costs rise more rapidly for a marginal decrease in climate impact.

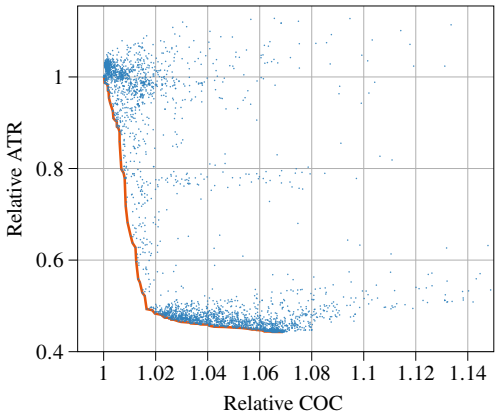

Fig. 13 Pareto front (orange line) between cost and climate objectives (data are normalized with respect to the cost-optimal aircraft, and blue dots are feasible designs).

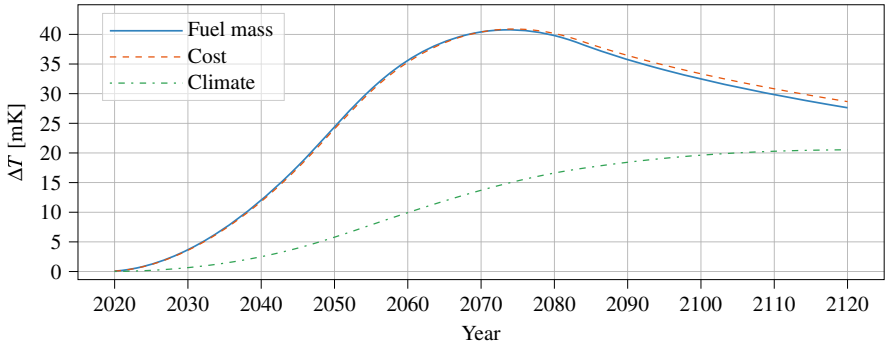

Fig. 12 Surface temperature change for the three objective functions.

D. Comparison with Literature

To put these results in perspective and highlight key findings, we compare the optimized designs with previous research by Dallara and Kroo [7] and Koch [13]. In essence, it can be concluded that the main design trends for climate-optimal aircraft are similar: lower cruise altitude at reduced Mach number, combined with a higher aspect ratio and bypass ratio, compared to cost-optimal aircraft. Dallara and Kroo [7] reported a reduction in ATR_{100} of 35 to 74%, depending on the discount rate (0 or 3%, respectively). In this study, the climate reduction is estimated to be approximately 57%, when assuming a discount rate of zero.

We expect that the main reason for this discrepancy in climate impact reduction is the difference in the contrail effects. The cost-optimal solution in this research has a relative contrail contribution of approximately 48%, whereas in the case of Dallara and Kroo [7], this contribution is only 17%. Hence, the achievable relative reduction becomes larger when the contrails vanish due to the lower cruise flight. The cost increase for the climate-optimal aircraft appears to be similar for both studies, as can be concluded from the Pareto fronts. This cost rise is approximately 6 to 10%. Small discrepancies may be the result of a different definition of the costs and distinct price assumptions. The ratio between fuel costs and time-related costs, such as salaries, especially performs an important role in this analysis.

Although the two studies are comparable, the current research also offers insight into the optimal engine parameters. For example, the trend in the OPR shows that climate-optimal aircraft do not feature a maximum OPR, presumably to lower the emission index of nitrogen oxides. The engine efficiency of the climate-optimal aircraft is also lower than for the fuel-optimal aircraft. This engine efficiency also performs a role in the contrail formation. Furthermore, due to span constraints, the aspect ratio cannot achieve values of 19 or 20, as is the case for the optimization by Dallara and Kroo [7]. This further limits the cruise efficiency of the climate-optimal aircraft and leads to a higher fuel burn. Nevertheless, considering current airport constraints and technology levels, this span constraint possibly makes the design more realistic.

V. Conclusions

This paper aims to research the relationship between designing for minimal climate impact and minimal operating costs. To this end, a multidisciplinary and multiobjective optimization framework is arranged to study the influence of wing, turbofan, and mission design variables on global warming impact (measured by the average temperature response) and direct operating costs, which are expressed in USDs. For a fixed fleet productivity level, it is estimated that the ATR_{100} can be reduced by approximately 57% when moving from the cost objective to the climate objective, at the expense of an 6.9% increase in operating costs. Although these values are based on a simplified analysis and are subject to uncertainties, it indicates that these objectives are indeed conflicting. The reduction in ATR_{100} can be achieved by lowering the cruise altitude to 7.6 km, flying at Mach 0.60, and by decreasing the engine overall pressure ratio as compared to the fuel-optimized case: from 57 to approximately 37. These changes are driven by non-CO_2 effects, namely, the emission of nitrogen oxides and the formation of contrails.

Flying slower causes the block time of the climate-optimized aircraft to be higher than for the aircraft designed for fuel burn or cost, which reduces its productivity as compared to these alternatives. For a hypothetical fleet with constrained productivity, it is concluded that approximately 13% more climate-optimized aircraft are needed than cost-optimized aircraft to achieve the same level of productivity on a fleet level.

Finally, four recommendations for further research can be formulated. First, the operational scenario can be made more realistic by assessing the aircraft performance and emissions for varying load factors and stage lengths. Operators deploy aircraft more flexibly, unlike the fixed mission in the current research. Second, it would be of interest to carry out this optimization for other aircraft categories, possibly with propeller technologies. Additionally, a simultaneous optimization of the aircraft design and mission trajectory is recommended to examine whether the climate impact can be reduced further. Finally, it has to be noted that the current framework employs a simplified climate model. Climate functions for aircraft design derived from more advanced models, as proposed in the GLOWOPT project, can offer a more accurate evaluation.

Appendix A: Input Data for Propulsion Discipline Verification and Validation

The conditions and data presented in Tables A1 and A2 [55,56] are adopted to model the General Electric GE90 engine for verification and validation purposes in Sec. III.A.

Appendix B: Input Data for Aircraft Synthesis Verification

Table B1 presents the top-level airplane requirements for the Airbus A320-200 and Boeing 777-200 aircraft employed for verification and validation in Sec. III.B.

Appendix C: Geometry Creation Methodology

Based on the design variables, a separate module creates a conceptual geometry of the aircraft employing empirical, statistical, and physics-based relations. Data from the geometry model propagate to

Table A1 Design requirements assumed for the GE90 engine model

Operating condition	Net thrust, kN	Altitude, km	Mach	ΔT_{ISA}, K
Cruise	77.85	10.67	0.80	0.00
Takeoff	376.80	0.00	0.00	15.00

Table A2 Design parameters assumed in the model of the GE90 engine at design point (cruise) [35,55,56]

Component	Parameter	Value	Unit
Inlet	Total pressure loss ΔP_T	0.980	— —
Fan	Bypass ratio	8.50	— —
	Total pressure ratio Π_{fan}	1.58	— —
	Polytropic efficiency η_{pol}	0.915	— —
Low-pressure compressor	Total pressure ratio Π_{lpc}	1.26	— —
	Polytropic efficiency η_{pol}	0.910	— —
High-pressure compressor	Total pressure ratio Π_{hpc}	20.0	— —
	Polytropic efficiency η_{pol}	0.900	— —
Combustor	Total pressure loss ΔP_T	0.950	— —
	Combustion efficiency η_{comb}	0.990	— —
	Turbine entry temperature	1430	K
High-pressure turbine	Polytropic efficiency η_{pol}	0.930	— —
	Mechanical efficiency η_{mech}	0.990	— —
Low-pressure turbine	Polytropic efficiency η_{pol}	0.930	— —
	Mechanical efficiency η_{mech}	0.990	— —

Table B1 Top-level airplane requirements employed for the aircraft synthesis verification and validation [48]

Requirement, unit	Airbus A320-200	Boeing 777-200
Maximum structural payload, tons	18.2	54.9
Harmonic range, 10^3 km (10^3 nm)	3200 (1730)	6000 (3200)
Cruise Mach number	0.78	0.84
Cruise altitude, km (FL)	11.3 (37)	11.9 (39)
Approach speed, m/s (kt)	70.0 (136)	70.0 (136)
Takeoff length (ISA conditions), m (ft)	2200 (7220)	2440 (8010)

FL = Flight level.

the aerodynamic and class-II mass estimation disciplines to compute the zero-lift drag component and structural mass, respectively. This appendix summarizes the methods used to create the conceptual outer line of the aircraft.

C.1. Fuselage

Because the passenger number and mission range are the main drivers for the fuselage, the geometry remains the same throughout the optimization iterations. This is because the inputs for the fuselage (namely, the top-level aircraft requirements (TLARs) and design assumptions per aircraft category) are held constant. The fuselage geometry methodology consists of three steps. First, the cabin cross section is designed. The number of seats abreast is determined from the maximum number of passengers $N_{\text{pax,max}}$, in an all-economy layout, according to the following relation:

$$N_{\text{seats abreast}} = \max(\lfloor 0.47 \cdot \sqrt{N_{\text{pax,max}}} \rfloor, 6) \tag{C1}$$

One aisle is introduced if the number of seats abreast is six or lower, whereas two aisles are considered for more seats. The required cabin width is then determined from a summation of seat and aisle widths by assuming the parameters in Table C1, which are derived from existing cabin layouts [49,50,57,58]. Based on the cabin width and the unit load device selection, the smallest possible inner cross-section radius is determined. To determine the outer diameter of the cross section d_{outer}, constant thicknesses are assumed according to the values in Table C1.

Second, the longitudinal layout of the fuselage is created. The interior of the fuselage consists of three parts: the cockpit, cabin, and tail. The total length of the fuselage is the sum of the lengths of these three sections. The number of rows multiplied by a statistical factor k_{cabin} determines the cabin length according to

$$N_{\text{rows}} = \frac{N_{\text{pax,max}}}{N_{\text{seats abreast}}} \tag{C2}$$

$$l_{\text{cabin}} = k_{\text{cabin}} \cdot N_{\text{rows}} \tag{C3}$$

The factor k_{cabin} also accounts for the length due to galley areas and exits. The total fuselage length follows by adding the cockpit length (assumed to be 4 m) and the tail length, which is assumed to be 1.6 times the outer cabin diameter.

Finally, the outer geometry of the fuselage is shaped. Similar to the inner layout, three distinct sections are considered: the nose cone, the central fuselage, and the tail cone. The nose and tail cones are longer than their respective interior sections, whereas the center fuselage is shorter than the cabin. For the nose cone, a fineness ratio of 1.3 with respect to d_{outer} is assumed, whereas for the tail cone, this ratio is three. Subsequently, the length of the central part is equal to the total length of the fuselage minus the lengths of the nose- and tail-cone sections.

The central section of the fuselage is assumed to be a cylinder with a diameter equal to d_{outer}. The nose-cone cross-sectional area decreases parabolically toward the nose point, which is located slightly below the fuselage center line according to a 4 deg droop angle measured from the front section of the central part. The tail cone starts tangentially to the central fuselage section and grows smoothly toward the tail point, which is located above the fuselage central line, taking into account an upsweep of 7 deg.

Table C1 Assumed parameters and design choices to determine the fuselage geometry

	Narrow-body ($\leq$ 6 seats abreast)	Wide-body (>6 seats abreast)
Seat width, m (in.)	0.457 (18.0)	0.457 (18.0)
Aisle width, m (in.)	0.457 (18.0)	0.584 (23.0)
Armrest width, m (in.)	0.05 (1.97)	0.05 (1.97)
Cabin length factor k_{cabin}	0.900	1.17
Cross-section d_{outer}, m (in.)	d_{inner} + 0.150 (5.91)	d_{inner} + 0.340 (13.4)
Loading device (LD)	LD3–LD45	2 × LD2 or LD3

C.2. Wing Planform

The design vector contains two variables that directly influence the wing geometry, namely, the aspect ratio and the wing loading. The wing surface area S follows from dividing (MTOM $\cdot$ g) by the wing loading. This area includes a trapezoidal section covered by the fuselage. The total wingspan b then results from the surface area and the aspect ratio. The area S and span b establish the main dimensions, but they do not fully define the wing planform. The other parameters required to conceptually determine the drag coefficient and structural mass are the quarter-chord sweep angle, the taper ratio, and the root- and tip-chord thicknesses.

In this study, it is assumed that the quarter-chord sweep angle $\Lambda_{0.25}$ is driven by the cruise Mach number according to the following statistical relationship for transport aircraft, based on data from Refs. [33,59]:

$$\Lambda_{0.25} = \begin{cases} 0 & \text{if } M_{\text{cr}} < 0.66 \\ \arccos\left(\dfrac{1.16}{M_{\text{cr}} + 0.5}\right) & \text{if } M_{\text{cr}} \geq 0.66 \end{cases} \tag{C4}$$

The taper ratio of the wing has to be adjusted according to the sweep angle to unload the tip section at higher sweep angles. Conceptually, the taper ratio can be related to the quarter-chord sweep angle as follows:

$$\lambda = -0.0083 \cdot \Lambda_{0.25} + 0.4597 \tag{C5}$$

Furthermore, the trailing-edge sweep angle is zero up to 30% of the semispan to facilitate easier integration of the landing gear and high-lift devices, which are placed perpendicular to the freestream flow direction. This assumption, combined with the aforementioned parameters, fully defines the top-view planform of the wing.

Although the exact three-dimensional outer mold line of the wing is not created, the aerodynamic and structural modules require an approximation of the root- and tip-chord thicknesses. The following relations provide such estimates [60]:

$$t/c_{\text{tip}} = \max\left(\min\left[\frac{\cos^3(\Lambda_{0.5}) \cdot [0.935 - (M_{\text{cr}} + 0.03) \cdot \cos(\Lambda_{0.5})] - 0.115 \cdot C_{L,\text{cr}}^{1.5}}{\cos^2(\Lambda_{0.5})}, 0.18\right], 0.10\right) \tag{C6}$$

$$t/c_{\text{root}} = t/c_{\text{tip}} + 0.03 \tag{C7}$$

The twist and dihedral angles are not considered in the current approach because the implemented methods are not sensitive to these parameters. The longitudinal position of the wing is determined

simultaneously with the empennage size. Therefore, this aspect is discussed in the subsequent section.

C.3. Empennage Planform and Wing Placement

The geometry module employs tail volume coefficients to determine the areas of the horizontal and vertical tail surfaces. The volume coefficients are derived from statistical data and are assumed to be independent of the design choices made by the optimizer. The respective surface areas, S_{ht} and S_{vt}, follow from the definitions of the volume coefficients for the horizontal $\bar{V}_{ht}$ and vertical $\bar{V}_{vt}$ tail:

$$\bar{V}_{ht} = \frac{(x_{ht} - x_{cg,aft})S_{ht}}{S \cdot \text{MAC}} \Rightarrow S_{ht} = \bar{V}_{ht} \cdot \frac{S \cdot \text{MAC}}{x_{ht} - x_{cg,aft}} \tag{C8}$$

$$\bar{V}_{vt} = \frac{(x_{vt} - x_{cg,aft})S_{vt}}{S \cdot b} \Rightarrow S_{vt} = \bar{V}_{vt} \cdot \frac{S \cdot b}{x_{vt} - x_{cg,aft}} \tag{C9}$$

In the preceding equations, x_{ht} and x_{vt} represent the longitudinal position of the aerodynamic center of the horizontal and vertical tails, respectively; whereas $x_{cg,aft}$ is the x coordinate of the most aft center-of-gravity position. The former two are set at 91 and 92% of the fuselage length, respectively. The statistical values for the tail volume coefficients are included in Table C2.

The operational c.g. excursion determines $x_{cg,aft}$ based on the position of the OEM c.g. location $x_{cg,OEM}$ and the varying locations of payload and fuel. However, to obtain $x_{cg,OEM}$, first, the longitudinal

Table C2 Assumed parameters and design choices to determine the empennage geometry

	Narrow body	Wide body
$\bar{V}_{ht}$	1.1	0.70
$\bar{V}_{vt}$	0.085	0.060
x_{fus}/l_{fus}	0.45	
x_{ht}/l_{fus}	0.91	
x_{vt}/l_{fus}	0.92	
x_{fe}/l_{fus}	0.45	
ξ_w	0.40	

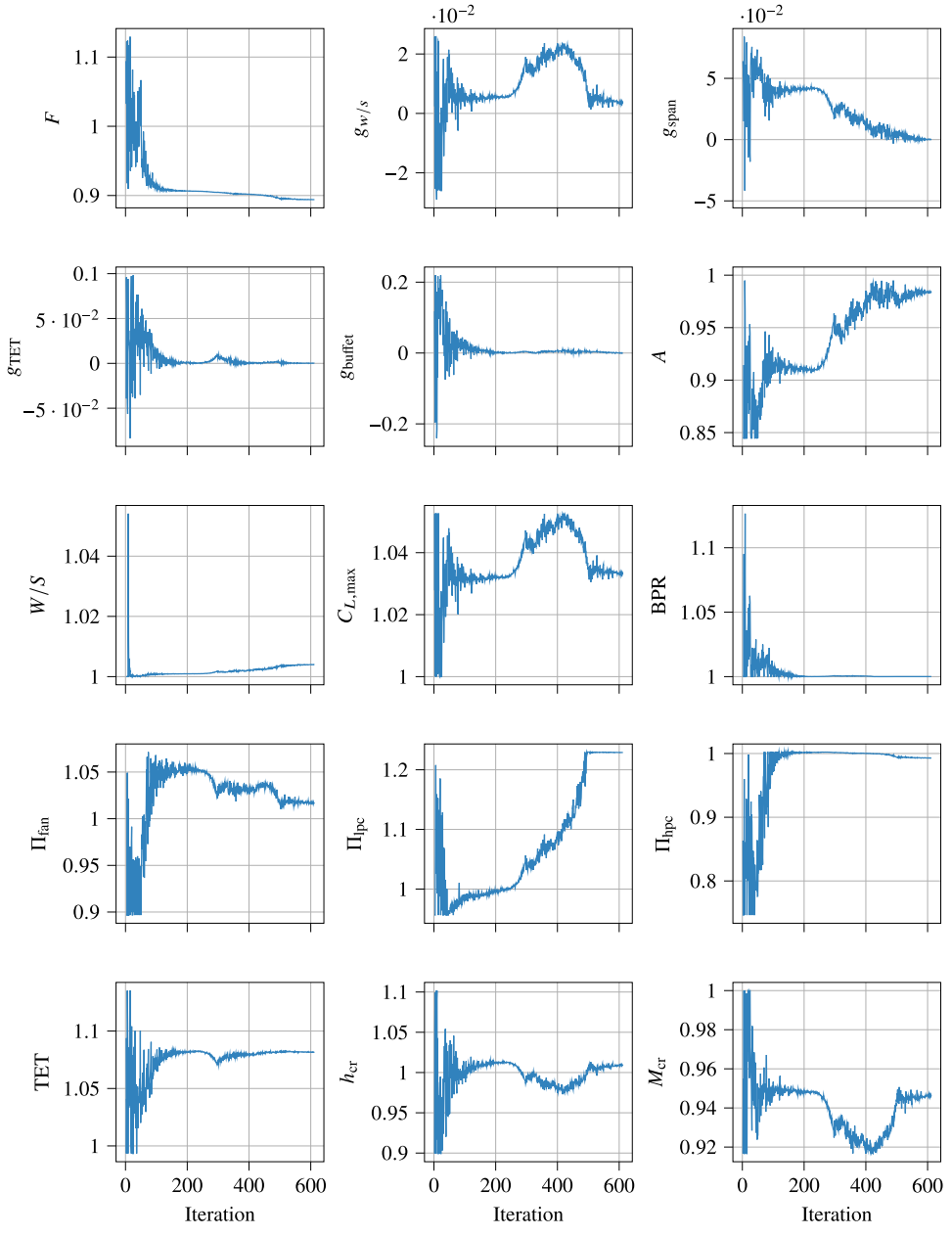

Fig. D1 Convergence plots of objective function, constraints, and design variables for fuel-mass minimization.

position of the wing has to be fixed. The latter position, defined by the leading edge of the MAC $x_{\mathrm{LE,MAC}}$, can be calculated from the masses of the main structural groups and their relative locations, as well the assumed position of the OEM c.g. location with respect to the mean aerodynamic chord: $\xi_{\mathrm{cg,OEM}} = 0.25$. Note that ξ is the longitudinal coordinate with respect to the mean aerodynamic chord [$\xi = (x - x_{\mathrm{LE,MAC}})/\bar{c}$]. The wing position $x_{\mathrm{LE,MAC}}$, measured from the fuselage nose point, is computed as follows:

$$x_{\mathrm{LE,MAC}} = x_{\mathrm{cg,FG}} + \bar{c} \cdot \left[\xi_{\mathrm{cg,WG}} \cdot \frac{m_{\mathrm{WG}}}{m_{\mathrm{FG}}} - \xi_{\mathrm{cg,OEM}} \cdot \left(1 + \frac{m_{\mathrm{WG}}}{m_{\mathrm{FG}}} \right) \right]$$

$$\text{where } x_{\mathrm{cg,FG}} = \frac{x_{\mathrm{fus}} m_{\mathrm{fus}} + x_{\mathrm{ht}} m_{\mathrm{ht}} + x_{\mathrm{vt}} m_{\mathrm{vt}} + x_{\mathrm{fe}} m_{\mathrm{fe}}}{m_{\mathrm{fus}} + m_{\mathrm{ht}} + m_{\mathrm{vt}} + m_{\mathrm{fe}}}, \quad \text{and}$$

$$\xi_{\mathrm{cg,WG}} = \frac{\xi_w m_w + \xi_{\mathrm{eng}} m_{\mathrm{eng}}}{m_w + m_{\mathrm{eng}}} \tag{C10}$$

The parameter $\bar{c}$ is the absolute length of the mean aerodynamic chord in the preceding equations. The masses of the groups [being the wing (w), fuselage (fus), engines (eng), empennage (ht and vt), and fixed equipment (fe)] result directly from the class-II mass estimation (Sec. II.B.3). The positions of the fuselage, empennage, and fixed equipment [fuselage group (FG)] are expressed relative to the fuselage length, whereas the locations of the wing and engine masses [wing group (WG)] are anchored to the MAC. The value of $x_{\mathrm{LE,MAC}}$ allows us to compute $x_{\mathrm{cg,OEM}}$ and $x_{\mathrm{cg,aft}}$, leading to the tail arms in Eqs. (C8) and (C9). The assumed relative positions in Eq. (C10) are gathered in Table C2. The relative position of the engines with respect to the MAC ξ_{eng} has to be determined for the design under consideration because it is dependent on the wing and engine parameters.

C.4. Nacelles

The nacelles around the turbofan engines have a cylindrical shape in the current model. Although this is a simplification, it provides the necessary data to estimate the drag contribution. The diameter of the nacelles is based on the fan diameter, which is estimated from the mass flow entering the engine according to the following relation:

$$d_{\mathrm{nac}} = 1.15 \cdot d_{\mathrm{fan}} = 1.15 \cdot 2 \cdot \sqrt{\frac{A_{\mathrm{fan}}}{\pi \cdot (1 - ht_{\mathrm{fan}}^2)}} \quad \text{with}$$

$$A_{\mathrm{fan}} = \dot{m}_{0,\mathrm{TOC}} \cdot \frac{\sqrt{T_{t2}}}{p_{t2} \cdot \mathrm{mfp}_2} \tag{C11}$$

In the preceding equation, ht_{fan} is the fan hub-to-tip ratio (0.33); $\dot{m}_{0,\mathrm{TOC}}$ is the total mass flow at top-of-climb conditions; and T_{t2}, p_{t2}, and mfp_2 are the total temperature, total pressure, and mass flow parameter [29] at the fan inlet face. The latter is calculated from the total temperature at this station and an axial Mach number of 0.6 [30]. The length of the nacelle, in meters, is computed from the following statistical relation provided by Torenbeek and Berenschot [61]:

$$l_{\mathrm{nac}} = 7.8 \left(\sqrt{\frac{\dot{m}_{0,\mathrm{TO}}}{\rho_0 \cdot a_0} \cdot \frac{1 + 0.2 \cdot \mathrm{BPR}_{\mathrm{TO}}}{1 + \mathrm{BPR}_{\mathrm{TO}}}} + 0.10 \right) \tag{C12}$$

Appendix D: Optimization Setup and Convergence

This appendix briefly discusses the optimization strategy employed to obtain the results in Sec. IV. The following three consecutive steps are carried out for the single-objective optimizations:

1) The design space is explored through design of experiments (DOE) using Latin hypercube sampling.

2) Global search algorithms are applied to the find design subspace that minimizes the objective under consideration. This helps with discrete steps in the design space, such as the formation condition of contrails. A genetic algorithm, or derived method, is used in this case.

3) The final step is to refine the optimal solution and ensure the solver converges. To achieve this, the Nelder–Mead algorithm is employed with a termination accuracy of 1.0×10^{-4} on the objective value. Although gradient-based methods, such as Sequential quadratic programming (SQP), also proved to be suitable for this step, the Nelder–Mead method appeared to be more robust.

The convergence in the final step is illustrated in Fig. D1 for the fuel-mass objective. Note that in this case, the optimizer decided the initial point with which the objective function and design variable values are normalized. Furthermore, the constraints are formulated such that the value of g has to be nonnegative. To obtain the Pareto front in Sec. IV.C, a multistrategy algorithm named pilOPT is employed, which is available in the modeFRONTIER software[‡]. This multiobjective algorithm automatically selects the best approach based on the problem formulation and DOE data, and it continues until not enough strictly dominating designs are found anymore.

Acknowledgments

This research is sponsored by the European Union's Clean Sky 2 Thematic Topics program (H2020-EU.3.4.5.10.) with grant agreement no. 865300. Thanks are extended to Feijia Yin for providing insight into turbine entry temperature limitations and to Peter Bos for critically reviewing the climate model and improving it.

References

[1] Lee, D., Pitari, G., Grewe, V., Gierens, K., Penner, J., Petzold, A., Prather, M., Schumann, U., Bais, A., Berntsen, T., Iachetti, D., Lim, L., and Sausen, R., "Transport Impacts on Atmosphere and Climate: Aviation," *Atmospheric Environment*, Vol. 44, No. 37, 2010, pp. 4678–4734.
https://doi.org/10.1016/j.atmosenv.2009.06.005

[2] Lee, D. S., Fahey, D. W., Skowron, A., Allen, M. R., Burkhardt, U., Chen, Q., Doherty, S. J., Freeman, S., Forster, P. M., Fuglestvedt, J., Gettelman, A., De León, R. R., Lim, L. L., Lund, M. T., Millar, R. J., Owen, B., Penner, J. E., Pitari, G., Prather, M. J., Sausen, R., and Wilcox, L. J., "The Contribution of Global Aviation to Anthropogenic Climate Forcing for 2000 to 2018," *Atmospheric Environment*, Vol. 244, Jan. 2021, Paper 117834.
https://doi.org/10.1016/j.atmosenv.2020.117834

[3] *Global Market Forecast: Cities, Airports and Aircraft, 2019–2038*, 5th ed., Airbus, S.A.S., Blagnac Cedex, France, Aug. 2019, pp. 10–11.

[4] *Commercial Market Outlook* 2019–2038, The Boeing Company, Chicago, IL, 2019.

[5] Antoine, N. E., and Kroo, I. M., "Framework for Aircraft Conceptual Design and Environmental Performance Studies," *AIAA Journal*, Vol. 43, No. 10, 2005, pp. 2100–2109.
https://doi.org/10.2514/1.13017

[6] Dahlmann, K., Koch, A., Linke, F., Lührs, B., Volker, G., Otten, T., Seider, D., Gollnick, V., and Schumann, U., "Climate-Compatible Air Transport System-Climate Impact Mitigation Potential for Actual and Future Aircraft," *Aerospace*, Vol. 3, 2016, Paper 38.
https://doi.org/10.3390/aerospace3040038

[7] Dallara, E. S., and Kroo, I., "Aircraft Design for Reduced Climate Impact," *49th AIAA Aerospace Sciences Meeting Including the New Horizons Forum and Aerospace Exposition*, AIAA Paper 2011-0265, 2011.
https://doi.org/10.2514/6.2011-265

[8] Grewe, V., Dahlmann, K., Flink, J., Frömming, C., Ghosh, R., Gierens, K., Heller, R., Hendricks, J., Jöckel, P., Kaufmann, S., Kölker, K., Linke, F., Luchkova, T., Lührs, B., Van Manen, J., Matthes, S., Minikin, A., Niklaß, M., Plohr, M., Righi, M., Rosanka, S., Schmitt, A., Schumann, U., Terekhov, I., Unterstrasser, S., Vázquez-Navarro, M., Voigt, C., Wicke, K., Yamashita, H., Zahn, A., and Ziereis, H., "Mitigating the Climate Impact from Aviation: Achievements and Results of the DLR WeCare Project," *Aerospace*, Vol. 4, No. 3, 2017, Paper 34.
https://doi.org/10.3390/aerospace4030034

[‡]Data available online at https://engineering.esteco.com/modefrontier [retrieved 16 February 2022].

[9] Henderson, R. P., Martins, J. R. R. A., and Perez, R. E., "Aircraft Conceptual Design for Optimal Environmental Performance," *Aeronautical Journal (1968)*, Vol. 116, No. 1175, 2012, pp. 1–22. https://doi.org/10.1017/S000192400000659X

[10] Chai, X., Yu, X., and Wang, Y., "Tradeoff Study Between Cost and Environmental Impact of Aircraft Using Simultaneous Optimization of Airframe and Engine Cycle," *International Journal of Aerospace Engineering*, Vol. 2017, May 2017, pp. 1–10. https://doi.org/10.1155/2017/2468535

[11] Egelhofer, R., Bickerstaff, C., and Bonnet, S., "Minimizing Impact on Climate in Aircraft Design," SAE International TP 2007-01-3807, Warrendale, PA, 2007. https://doi.org/10.4271/2007-01-3807

[12] Wang, Y., Xing, Y., Yu, X., and Zhang, S., "Flight Operation and Airframe Design for Tradeoff Between Cost and Environmental Impact," *Journal of Aerospace Engineering*, Vol. 232, No. 5, 2018, pp. 973–987. https://doi.org/10.1177/0954410017748967

[13] Koch, A., "Climate Impact Mitigation Potential Given by Flight Profile and Aircraft Optimization," Dissertation, Technischen Univ. Hamburg-Harburg, Hamburg, Germany, Nov. 2013. https://doi.org/10.13140/RG.2.1.4896.9047

[14] Grewe, V., and Stenke, A., "AirClim: An Efficient Tool for Climate Evaluation of Aircraft Technology," *Atmospheric Chemistry and Physics*, Vol. 8, No. 16, 2008, pp. 4621–4639. https://doi.org/10.5194/acp-8-4621-2008

[15] Schutte, J., and Mavris, D. N., "Evaluation of N+2 Technologies and Advanced Vehicle Concepts," *53rd AIAA Aerospace Sciences Meeting*, AIAA Paper 2015-0514, 2015. https://doi.org/10.2514/6.2015-0514

[16] Air Travel–Greener by Design, "Air Travel—Greener by Design Mitigating the Environmental Impact of Aviation: Opportunities and Priorities," *Aeronautical Journal (1968)*, Vol. 109, No. 1099, 2005, pp. 361–416. https://doi.org/10.1017/S0001924000000841

[17] Herbon, J., Aicholtz, J., Hsieh, S.-Y., Viars, P., Birmaher, S., Brown, D., Patel, N., Carper, D., Cooper, C., and Fitzgerald, R., "N+2 Advanced Low NOx Combustor Technology Final Report," NASA CR-2017-219410, 2017.

[18] Schumann, U., "Influence of Propulsion Efficiency on Contrail Formation," *Aerospace Science and Technology*, Vol. 4, No. 6, 2000, pp. 391–401. https://doi.org/10.1016/S1270-9638(00)01062-2

[19] Reynolds, T., Barrett, S., Dray, L., Evans, A., Köhler, M., Vera-Morales, M., Schäfer, A., Wadud, Z., Britter, R., Hallam, H., and Hunsley, R., "Modelling Environmental and Economic Impacts of Aviation: Introducing the Aviation Integrated Modelling Project," *7th AIAA ATIO Conference, 2nd CEIAT International Conference on Innovation and Integration in Aero Sciences, 17th LTA Systems Technology Conference, Followed by 2nd TEOS Forum*, AIAA Paper 2007-7751, 2007. https://doi.org/10.2514/6.2007-7751

[20] Bernardo, J. E., Zaidi, T., LeVine, M., Jimenez, H., and Mavris, D., "Rapid Integrated Interdependent Fleet-Level Environmental Model," *Journal of Aircraft*, Vol. 54, No. 3, 2017, pp. 939–954. https://doi.org/10.2514/1.C033572

[21] LeVine, M. J., Bernardo, J. E., Kirby, M., and Mavris, D. N., "Average Generic Vehicle Method for Fleet-Level Analysis of Noise and Emission Tradeoffs," *Journal of Aircraft*, Vol. 55, No. 3, 2018, pp. 929–946. https://doi.org/10.2514/1.C034368

[22] Vera-Morales, M., and Hall, C. A., "Modeling Performance and Emissions from Aircraft in the Aviation Integrated Modelling Project," *Journal of Aircraft*, Vol. 47, No. 3, 2010, pp. 812–819. https://doi.org/10.2514/1.44020

[23] Moolchandani, K., Govindaraju, P., Roy, S., Crossley, W. A., and DeLaurentis, D. A., "Assessing Effects of Aircraft and Fuel Technology Advancement on Select Aviation Environmental Impacts," *Journal of Aircraft*, Vol. 54, No. 3, 2017, pp. 857–869. https://doi.org/10.2514/1.C033861

[24] Jimenez, H., Pfaender, H., and Mavris, D., "Fuel Burn and CO2 System-Wide Assessment of Environmentally Responsible Aviation Technologies," *Journal of Aircraft*, Vol. 49, No. 6, 2012, pp. 1913–1930. https://doi.org/10.2514/1.C031755

[25] McEnteggart, Q., and Whidborne, J. F., "Multiobjective Environmental Departure Procedure Optimization," *Journal of Aircraft*, Vol. 55, No. 3, 2018, pp. 905–917. https://doi.org/10.2514/1.C033132

[26] Mori, R., "Fuel-Saving Climb Procedure by Reduced Thrust near Top of Climb," *Journal of Aircraft*, Vol. 57, No. 5, 2020, pp. 800–806. https://doi.org/10.2514/1.C035200

[27] Lührs, B., Niklass, M., Froemming, C., Grewe, V., and Gollnick, V., "Cost-Benefit Assessment of 2D and 3D Climate and Weather Optimized Trajectories," *16th AIAA Aviation Technology, Integration, and Operations Conference*, AIAA Paper 2016-3758, 2016. https://doi.org/10.2514/6.2016-3758

[28] Hwang, J. T., Jasa, J. P., and Martins, J. R. R. A., "High-Fidelity Design-Allocation Optimization of a Commercial Aircraft Maximizing Airline Profit," *Journal of Aircraft*, Vol. 56, No. 3, 2019, pp. 1164–1178. https://doi.org/10.2514/1.C035082

[29] Mattingly, J. D., Heiser, W. H., and Pratt, D. T., *Aircraft Engine Design*, 2nd ed., AIAA, Reston, VA, 2002. https://doi.org/10.2514/4.861444

[30] Obert, E., *Aerodynamic Design of Transport Aircraft*, IOS Press, Amsterdam, 2009.

[31] Lambe, A. B., and Martins, J. R., "Extensions to the Design Structure Matrix for the Description of Multidisciplinary Design, Analysis, and Optimization Processes," *Structural and Multidisciplinary Optimization*, Vol. 46, No. 2, 2012, pp. 273–284. https://doi.org/10.1007/s00158-012-0763-y

[32] Roskam, J., *Airplane Design. Part I: Preliminary Sizing of Airplanes*, DARcorporation, Lawrence, KS, 1985.

[33] Torenbeek, E., *Synthesis of Subsonic Airplane Design*, Delft Univ. Press and Kluwer Academic Publ., Dordrecht, The Netherlands, 1982.

[34] Walsh, P. P., and Fletcher, P., *Gas Turbine Performance*, 2nd ed., Blackwell Science, Oxford, England, U.K., 2004, pp. 113–119. https://doi.org/10.1002/9780470774533

[35] Greitzer, E. M., Bonnefoy, P., de la Rosa Blanco, E., Dorbian, C., Drela, M., Hall, D., Hansman, R., Hileman, J., Liebeck, R., Lovegren, J., Mody, P., Pertuze, J., Sato, S., Spakovszky, Z., Tan, C., Hollman, J., Duda, J., Fitzgerald, N., Houghton, J., Kerrebrock, J., Kiwada, G., Kordonowy, D., Parrish, J., Tylko, J., Wen, E., and Lord, W., "N+3 Aircraft Concept Designs and Trade Studies. Volume 2: Appendices—Design Methodologies for Aerodynamics, Structures, Weight, and Thermodynamic Cycles," NASA CR-2010-216794/VOL2, 2010.

[36] Torenbeek, E., "The Initial Calculation of Range and Mission Fuel During Conceptual Design," Faculty of Aerospace Engineering, Delft Univ. of Technology TR LR-525, Delft, The Netherlands, 1987.

[37] Grewe, V., and Dahlmann, K., "How Ambiguous are Climate Metrics? And Are We Prepared to Assess and Compare the Climate Impact of New Air Traffic Technologies?" *Atmospheric Environment*, Vol. 106, April 2015, pp. 373–374. https://doi.org/10.1016/j.atmosenv.2015.02.039

[38] Sausen, R., and Schumann, U., "Estimates of the Climate Response to Aircraft CO_2 and NO_x Emissions Scenarios," *Climate Change*, Vol. 44, Jan. 2000, pp. 27–58. https://doi.org/10.1023/A:1005579306109

[39] Climate Change 2007—The Physical Science Basis. Working Group I. Contributions to the Fourth Assessment Report of the Intergovernmental Panel of Climate Change, IPCC, Cambridge Univ. Press, New York, 2007, p. 104, https://www.ipcc.ch/report/ar4/syr/.

[40] Ponater, M., Pechtl, S., Sausen, R., Schumann, U., and Hüttig, G., "Potential of the Cryoplane Technology to Reduce Aircraft Climate Impact: A State-of-the-Art Assessment," *Atmospheric Environment*, Vol. 40, No. 36, 2006, pp. 6928–6944. https://doi.org/10.1016/j.atmosenv.2006.06.036

[41] Schwartz Dallara, E., Kroo, I. M., and Waitz, I. A., "Metric for Comparing Lifetime Average Climate Impact of Aircraft," *AIAA Journal*, Vol. 49, No. 8, 2011, pp. 1600–1613. https://doi.org/10.2514/1.J050763

[42] Fahey, D. W., Baughcum, S. L., Gupta, M., Lee, D. S., Sausen, R., and van Velthoven, P., "Aviation and Climate: State of Science," International Civil Aviation Organization (ICAO) TR, Montreal, 2013, pp. 48–53, https://www.icao.int/environmental-protection/Documents/EnvironmentalReports/2013/ICAOEnvReport2013.pdf [accessed 7 June 2022].

[43] Schwartz Dallara, E., "Aircraft Design for Reduced Climate Impact," Dissertation, Stanford Univ., Stanford, CA, Feb. 2011.

[44] Grewe, V., Matthes, S., and Dahlmann, K., "The Contribution of Aviation NO_x Emissions to Climate Change: Are We Ignoring Methodological Flaws?" *Environmental Research Letters*, Vol. 14, No. 12, 2019, Paper 121003. https://doi.org/10.1088/1748-9326/ab5dd7

[45] Sonntag, D., "Important New Values of the Physical Constants of 1986, Vapour Pressure Formulations Based on the ITS-90, and Psychrometer Formulae," *Zeitschrift für Meteorologie*, Vol. 40, No. 5, 1990, pp. 340–344.

[46] Roskam, J., *Airplane Design, Part VIII: Airplane Cost Estimation: Design, Development, Manufacturing and Operating*, DARcorporation, Lawrence, KS, 1985, Chap. 5.

[47] Nicolai, L. M., and Carichner, G. E., *Fundamentals of Aircraft and Airship Design*, Vol. 1, AIAA, Reston, VA, 2010. https://doi.org/10.2514/4.867538

[48] Jenkinson, L. R., Simpkin, P., and Rhodes, D., *Civil Jet Aircraft Design*, Arnold, London, 1999. https://doi.org/10.2514/4.473500

[49] "Airbus A320 Aircraft Characteristics Airport and Maintenance Planning," Airbus, S.A.S., Customer Services TR, Blagnac, 2019.

[50] "Boeing 777-200/300 Airplane Characteristics and Airport Planning," Boeing Commercial Airplanes TR D6-58329, Chicago, IL, 2002.

[51] Swelbar, W. S., and Belobaba, P. P., *Airline Data Project* [online database], Massachusetts Inst. of Technology, Cambridge, MA, http://web.mit.edu/airlinedata/www/default.html [retrieved 27 Nov. 2020].

[52] Husemann, M., Schäfer, K., and Stumpf, E., "Flexibility Within Flight Operations as an Evaluation Criterion for Preliminary Aircraft Design," *Journal of Air Transport Management*, Vol. 71, Aug. 2018, pp. 201–214. https://doi.org/10.1016/j.jairtraman.2018.04.007

[53] Köler, M. O., Rädel, G., Dessens, O., Shine, K. P., Rogers, H. L., Wild, O., and Pyle, J. A., "Impact of Perturbations to Nitrogen Oxide Emissions from Global Aviation," *Journal of Geophysical Research: Atmospheres*, Vol. 113, 2008, Paper D11305. https://doi.org/10.1029/2007 JD009140

[54] Jeßberger, P., Voigt, C., Schumann, U., Sölch, I., Schlager, H., Kaufmann, S., Petzold, A., Schäuble, D., and Gayet, J.-F., "Aircraft Type Influence on Contrail Properties," *Atmospheric Chemistry and Physics*, Vol. 13, No. 23, 2013, pp. 11,965–11,984. https://doi.org/10.5194/acp-13-11965-2013

[55] "General Electric GE90," *Jane's Aero-Engines*, IHS Markit, 2019, https://customer.janes.com/Janes/Display/JAE_0735-JAE_.

[56] York, M. A., Hoburg, W. W., and Drela, M., "Turbofan Engine Sizing and Tradeoff Analysis via Signomial Programming," *Journal of Aircraft*, Vol. 55, No. 3, 2018, pp. 988–1003. https://doi.org/10.2514/1.C034463

[57] "Boeing 737 Airplane Characteristics and Airport Planning," Boeing Commercial Airplanes TR D6-58325-6, Chicago, IL, 2013.

[58] "Airbus A350 Aircraft Characteristics Airport and Maintenance Planning," Airbus S.A.S. Customer Services TR, Blagnac, 2020.

[59] Raymer, D., *Aircraft Design: A Conceptual Approach*, AIAA, Reston, VA, 2012.

[60] Torenbeek, E., *Advanced Aircraft Design: Conceptual Design, Technology and Optimization of Subsonic Civil Airplanes*, Wiley, Chichester, England, U.K., 2013. https://doi.org/10.1002/9781118568101

[61] Torenbeek, E., and Berenschot, G., "De Berekening van het Omspoeld Gondeloppervlak van Enkel- en Dubbelstroom Straalmotoren voor Civiele Vliegtuigen," Faculty of Aerospace Engineering, Delft Univ. of Technology TR M-445, Delft, The Netherlands, 1983.